Simen Aase
Simen Bekkevoll
Sigmund A.K. Forberg

A Model Based Parametric Study of Alumina Feeding and Dissolution

Bachelor's project

NTNU
Norwegian University of
Science and Technology

A Model Based Parametric Study
of Alumina Feeding and Dissolution

Thesis for the degree of Bachelor in Engineering

Trondheim, June 2020

Norwegian University of Science and Technology
Faculty of Natural Sciences
Department of Material Science and Engineering

Written by

Simen Bekkevoll

Simen Aase

Sigmund A.K. Forberg

Supervised by

Kristian Etienne Einarsrud

Sindre Engzelius Gylver

◉ NTNU | Norwegian University of
Science and Technology

Abstract

In the Hall-Hèroult process, alumina (Al_2O_3) is used as the raw material in the energy-intensive production of aluminium, where alumina powder is fed into a bath mainly consisting of molten cryolite. Environmental challenges in the industrial electrolysis cell makes some phenomena affecting the process hard to fully investigate, thus physical models in laboratories are often used for research. A faster dissolution of alumina, with an efficient feeding and dispersion of the powder, has several benefits for the process. This thesis conducts a model based parametric study of alumina feeding and dissolution, where the effect of variations in temperature, particle size distribution (PSD) and gas evolution are considered. The experiments were carried out in a water model and recorded for documentation. Every recorded experiment was thoroughly processed and the results are presented as charts where surface area of the floating powder is plotted against the floating time.

Investigations on determining a powder to simulate alumina in the water model was conducted in the initial experiments, with the discovery of crushed Natreen sprinkle sugar as a well-suited outcome. Optimizing the water model to increase its resemblance to industrial cells were also performed during these experiments.

Results from the water model tests showed the importance of the PSD upon floating time. A PSD with a high amount of fines increased the floating time significantly and gave a mean floating time between 240 to 550 seconds. In comparison, the PSD with a small amount of fines had a mean floating time in the range of 35 to 135 seconds. It was also indicated through Minitab results that an increase in temperature and gas flow had positive effects on the dissolution rate, meaning a reduction in floating time.

It was concluded that the work regarding powder determination and model optimization was successful and results which indicated similarities with previous studies were obtained. Though measures were taken, a fully automated image analysis was not achieved.

Suggestions for future research on water model experiments are presented, with the focus on a more precise PSD management for the powder used and the overall conditions that may lead to a more automated image analysis.

I

Sammendrag

Alumina (Al_2O_3) blir brukt som råmateriale i den energikrevende Hall-Hèroult-prosessen for produksjon av aluminium. I denne prosessen blir aluminapulver matet til et kryolittbad med jevne mellomrom. Det utfordrende miljøet i den industrielle elektrolysen gjør det vanskelig å studere enkelte fenomener som påvirker prosessen. Fysiske modeller blir av den grunn ofte brukt i forskning på området. Energikravet til prosessen vil kunne reduseres ved hjelp av raskere innløsning, samt mer effektiv mating og spredning. Denne oppgaven omhandler en modellbasert parametrisk studie av mating og innløsning av alumina, med fokus på effekten av variasjon i temperatur, partikkelstørrelsesfordeling (PSD), og gassutvikling. Eksperimentene ble gjennomført i en vannmodell og dokumentert med videokameraer. Hvert forsøk ble grundig prosessert ved hjelp av bildebehandlingsprogramvare, før resultatene ble presentert som grafer der overflatearealet til pulveret ble plottet mot flytetiden.

I løpet av de innledende eksperimentene ble det utført undersøkelser rundt pulverfast-settelse til vannmodell forsøkene for å simulere alumina, med Natreen strøsukker som et velegnet resultat. Optimalisering av vannmodellen for å øke dens likhet til industrielle celler ble også utført under disse eksperimentene.

Resultatene fra vannmodellen viste viktigheten av PSD i forhold til flytetid. PSD med en stor andel fine partikler ga økt flytetid med gjennomsnitt mellom 240 og 550 sekunder. Eksperimentene med en lavere andel fine partikler viste en gjennomsnittlig flytetid mellom 35 og 135 sekunder. Resultatene indikerer i tillegg at en økning i temperatur og gassutvikling vil gi raskere innløsning og redusert flytetid.

Det ble konkludert med at valg av pulver og modelloptimalisering har vært vellykket, samt at det har blitt oppnådd resultater i vannmodellen med likheter til tidligere studier. En hel-automatisert metode for etterbehandling av videoer ble ikke oppnådd, ettersom lysforhold viste seg å være en større utfordring enn først antatt.

Til slutt er det lagt frem forslag til videre arbeid. Disse har fokus på mer nøyaktig kontroll av PSD og nærmere undersøkelser av hvilke faktorer som kan bidra til automatisering av bildebehandlingen.

Acknowledgments

Contents

CONTENTS

List of Figures

List of Tables

List of Terms

CE   current efficiency.

NIH   National Institutes of Health.

PAH   polycyclic aromatic hydrocarbon.

PFC   perfluorocarbon.

PSD   particle size distribution.

SEM   scanning electron microscope.

SGA   smelter grade alumina.

UNM   University of New Mexico.

USD   United States dollar.

wt%   percentage by weight.

1 Introduction

Aluminium is the third most abundant element in the earth's crust (8 wt%), always bound with oxygen and in combination with silicon or other metals [1, p.26]. It is a commonly used material, having a wide range of usage in today's society (e.g., kitchen appliances, cans, aeroplanes) [1]. Two independent processes are used in aluminium production. From the bauxite-ore to alumina (Al_2O_3) by the Bayer process (1888), and from alumina to aluminium in the Hall-Héroult process (1886) [2, p.49]. These energy-intensive processes are a fundamental part of aluminium production, with many improvements through the years regarding reduction in emissions and energy-consumption.

1.1 Aluminium production process

In the Hall-Héroult process, aluminium is produced when powder of aluminium oxide, commonly called alumina, is dissolved in a bath of molten cryolite and reacts with carbon in the following electrochemical reaction:

$$2\,Al_2O_{3(d)} + 3\,C_{(s)} \longrightarrow 4\,Al_{(l)} + 3\,CO_{2(g)} \tag{1.1}$$
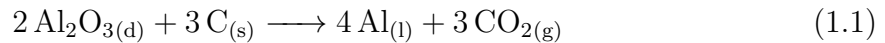
Alumina is the raw material used in the process, and with continuous consumption of carbon, pure aluminium and carbon dioxide is produced. Electric current reduces the aluminium cations into the molten metal, resting on the bottom of the cell, right below the electrolyte. An illustration of a typical modern aluminium cell is displayed in Figure 1.1. Oxygen from the alumina reacts with the carbon from the anodes submerged in the bath, as shown in Eq. (1.2) [2, p.57].

$$2\,O^{2-}_{(c)} + C_{(s)} \longrightarrow CO_{2(g)} + 4\,e^- \tag{1.2}$$
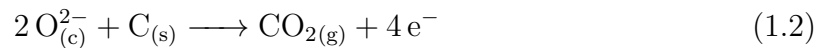
Eq. (1.1) illustrates the theoretical stochiometric ratio of produced aluminium. To produce 1 kg of aluminium, 1.89 kg of Al_2O_3 should react with 0.33 kg of solid carbon and produce 1.22 kg of CO_2. In practice, however, the actual values are 1.93 kg Al_2O_3 reacting with 0.40-0.45 kg of solid carbon, resulting in a total of 1.5 kg CO_2 per kg Al produced [2, p.50].
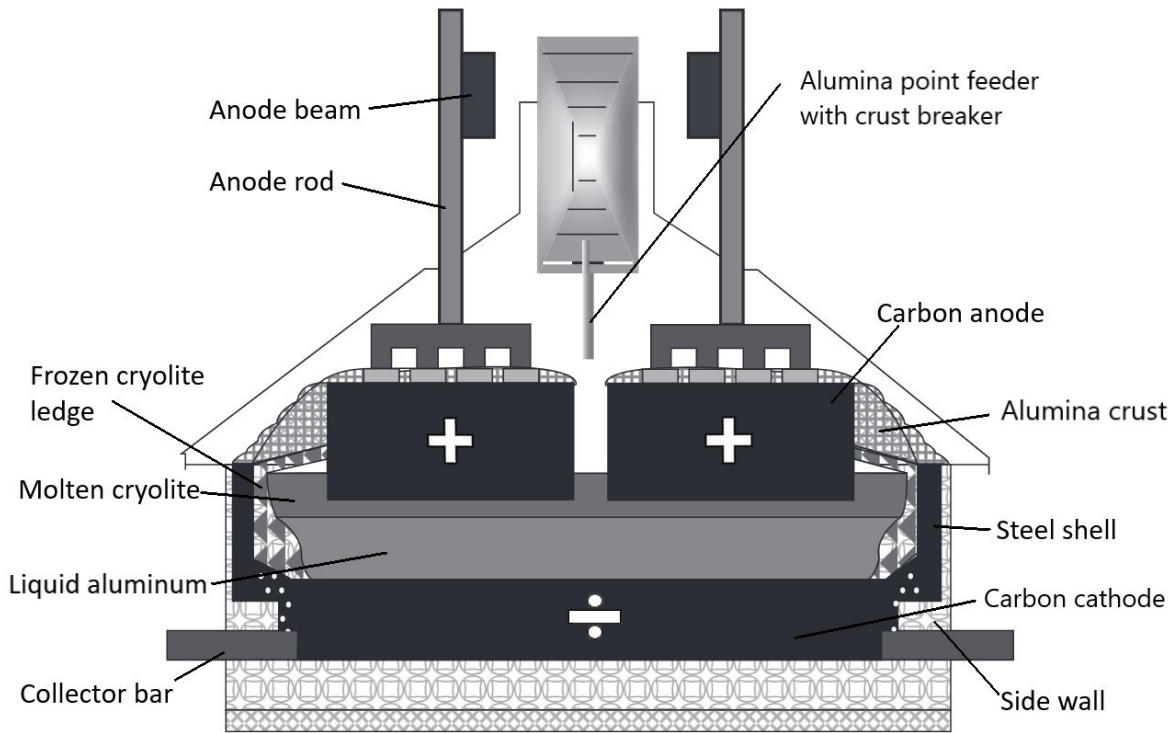
Figure 1.1: Schematic drawing of an aluminium cell.
[2, p.58]

Most of the aluminium production process today is controlled by automated systems and instruments. Manual operations are limited to anode changing, and the tapping of bath and metal. Anode change is performed daily due to continuous consumption of carbon. The anode is consumed at a rate of 1.5 cm/day, resulting in a reduction between one-third and one-fourth of its size during their lifetime, which is between 20-25 days upon replacement [3, p.201]. Anode replacement is performed one at a time, but changing patterns may vary between different smelters. Replaced anodes are called butts, and are recycled into new anodes.

Metal produced in the cells needs to be collected in regular time intervals, typically between 24 and 48 hours, in order to maintain stable operating conditions. Molten metal is collected in large cast iron crucibles by a siphon nozzle placed into the cell at a specific depth. The tip of the tapping tube must not be put too deep or above the metal pad, in order to prevent mixing of bath and metal or damaging the carbon lining. Vacuum is generated in the tube by an air-ejection system connected to a compressed air supply. The metal is then sucked into a crucible through the tube [4]. When the

crucible is filled to its maximum capacity, it is transported to a cast house for further treatment. Constant presence of metal in the cell is crucial, as it works as a part of the cathode and protects the carbon lining underneath the metal pad from direct contact with bath. Higher levels of molten metal can cause sludge. Sludge is a viscous two-phase mixture of undissolved alumina and bath located at the bottom of the cell underneath the metal pad. This is an unwanted effect, as it disturbs the movement of the metal and bath, and can insulate the electrical connection between the carbon cathode and the metal pad. However, this effect is not harmful as long as there is no build-up of sludge. The height of the metal pad can change up to 2 cm/day which is enough to change the heat balances in the cell to exceed the tolerance limit for stable operation conditions [3].

1.1.1 Anodes and anode material

There are two types of anodes used in aluminium production: prebaked and Söderberg. The prebaked anodes, displayed in Figure 1.1, are mostly used for better power efficiency and lower polycyclic aromatic hydrocarbon (PAH) emissions [2, p.54] [5]. Prebaked anodes mainly consist of calcinated and crushed petroleum coke mixed with tar-pitch as a binding material. The anode material is shaped into blocks and baked in a special furnace. To provide electric contact and physical support, an aluminum or copper rod is mounted to an iron yoke with stubs. These stubs are then molded into cavities on top of the anode by applying cast iron or rammed paste around the stubs [2, p.53]. High purity carbon is desired for the prebaked anodes, as contamination of impurities may lead to anode damage or unnecessary use of electric power. Impurities such as phosphorus can be accumulated in the electrolyte and consume electric current by cyclic red-ox reactions [2, p.53].

1.1.2 Cathode and cathode material

The cathode of an aluminium cell is introduced in the top surface of the metal pad and ends at the steel collector bars in the bottom of the cell. The bottom of the cell and side walls are made of various compounds, but mainly consist of prebaked carbon blocks seamed together by a layer of carbonaceous ramming paste [2, s.53]. Molten aluminium needs to be in direct contact with the bottom of the cell to maintain electrical contact, while the side walls are covered by a protective layer of frozen bath. The steel shell surrounding the cell contributes to heat loss control. A steel collector bar is molded into the carbon cathode to conduct electric current from the cell [2, p.57].

1.1.3 Electrolyte

The electrolyte is one of the main components in the production of aluminium and mainly consists of liquid cryolite (Na_3AlF_6).

The main function of the electrolyte is to be a solvent for the added alumina. Further, the electrolyte functions as a conductive medium, whilst also providing a physical separating layer between the anode and cathode. To maintain the self-heating properties of the cell, the electrolyte needs to provide a heat-generating resistance [2, p.56].

Properties of the electrolyte

A positive effect of using cryolite is the density difference between the electrolyte and liquid aluminium (2.1 kg/L compared to 2.3 kg/L), making the electrolyte float on top the aluminium [2, p.56]. Fluoride additives are added to increase efficiency of the process. Aluminum fluoride (AlF_3), calcium fluoride (CaF_2), lithium fluoride (LiF) and magnesium fluoride (MgF_2) are often used, changing the physical and chemical properties of the bath. Reducing the melting temperature of the bath and increasing current efficiency (CE) are some of the major benefits of additives. The composition of additives in the bath may vary between different smelters, but all additives listed above reduces the solubility of alumina [3, p.50-58].

Magnetic hydrodynamics and convection of the bath

In the electrolyte and metal pad there are two main factors that generate convection in the bath: magnetic fields, and gas bubbles generated beneath the anodes. Other natural convection sources, such as temperature gradients and composition differences in the electrolyte, have insignificant impact compared to magnetic fields and gas bubbles [2, p.60].

In aluminium cells, large electric currents generates a strong magnetic field between them. Lorentz forces are applied when these magnetic fields interact with the high electric current, producing movement of liquid conductors [2, p.60].

The strong magnetic field generates three different types of disturbances in the metal pad:

1. Vertical displacement.
2. Circulating flow with relatively high velocities.
3. Internal wave motion.

The waves generated in the bath may lead to electrical short circuiting if the metal pad reaches the anodes. The circulating flow may cause height variations of the metal pad, high metal velocities and instabilities in the bath. The dominant force of movement in the electrolyte comes from gas bubbles produced beneath the anodes, whereas the metal pad movements from electromagnetic forces are predominate [2, p.61].

To compensate for the electromagnetic forces and reduce undesirable disturbance in the bath, an advanced electrical busbar system is designed for the interconnecting cell lines. The magnetic fields and flow patterns of the electric current are complicated which makes design and calculations of the busbar system challenging [2, p.61].

During normal cell operation the bath usually has a temperature between 955-965°C while cryolite with additives has a melting temperature 5-10°C lower. The temperature difference is called *superheat*. The superheat controls the thickness of the cryolite layer used as cell linings, which is why the attention of the superheat phenomena has increased in recent years [2, p.50]. Additionally, for an effective production process, the amount of energy used to increase superheat temperature is considered a waste of energy [3, p.50].

1.2   Alumina and alumina feeding

Alumina is a white powder that looks like table salt, has a very high melting point (2050°C) and is highly absorbent. In industrial cells, alumina, in addition to being the raw material of the process and the absorbent in the dry scrubbers, contributes as a thermal insulator. A self-forming crust consisting of bath and alumina is situated on top of the anodes and above the electrolyte (see Figure 1.1) to conserve heat from the cell [2, p.50].

Elder aluminium cell designs had infrequent addition of alumina from the side of the cell. Modern aluminium cells have strategically placed point-feeders inside the cells, facilitating addition of alumina to the bath at constant rates [2, p.50]. It is important for the production process that the small amounts of added alumina is quickly dissolved and mixed with the electrolyte, in order to maintain a continuous concentration of alumina in the bath [6].

Temperature differences between fed alumina and the bath causes formations of rafts when the electrolyte freezes around alumina particles. The formation of these rafts

is undesirable as they hinder the dissolution of alumina, thereby reducing alumina concentrations in the bath and potentially causing unwanted anode effects [6]. Larger rafts may sink below the metal pad to form sludge [6]. These disturbances decrease the efficiency of the aluminium production process, and therefore, a better understanding of the mechanisms behind raft formation and dissolution is desirable.

1.3   Energy efficiency

Aluminium production requires a large amount of electrical energy which is the product of voltage (U) and electric charge (Q):

$$W = U \times Q \tag{1.3}$$

The price of electrical energy has steadily increased through the years, making the aluminium production process more expensive [6]. Ideally, it is preferable for energy used in the process to be supplied from renewable sources rather than energy sourced from fossil fuels [1]. To maintain an efficient production process, cell voltage must be minimized and current efficiency maximized. In recent years, smelters have increased the amperage of their cells to reduce cell voltage in order to achieve nearly constant heat input to the cells [2, p.60]. Reduced interpolar distance and increasing anode sizes are the main contributors, reducing available bath volume for alumina to dissolve in [6].

Interpolar distance, the distance between the anodes and the cathode, determines cell voltage. Consequently, reducing the interpolar distance decreases the voltage. Voltage is mainly lost in the bath due to ohmic resistance between anode and cathode, but some of the losses occur in the anode and cathode material as well [3, p.22]. Reduction in the interpolar distance is limited to about 4 cm to avoid short-circuiting and extensive back-reactions, thus limiting further amperage increase [3, p.26].

Since aluminium plants are often of substantial size, small innovations regarding an increased CE will further reduce energy-consumption and emissions on a larger scale. The CE represents the effectiveness in utilization of power in the process. This is the ratio between actual and theoretical production rates and displays the amount of current specifically used to produce aluminium.

$$CE = \frac{P(Al)_{Actual}}{P(Al)_{Theoretical}} \times 100\% \qquad (1.4)$$

In every electrochemical process, there are some losses due to various factors that will reduce the CE. Inadequate alumina concentrations have a negative influence on CE through back reactions and anode effects, further motivating this work [3, p.155].

1.4 Objectives

The purpose of this thesis is to conduct and document a model based parametric study of alumina feeding and dissolution. It will focus on the raft formations that occur when alumina is fed and dispersed into molten cryolite, and the industrial parameters affecting rapid dissolution. To conduct research on raft formation and its behavior, experiments and observations will be performed in a water model built for this purpose. The water model provides the opportunity to run experiments in a safe environment without having to consider the harsh conditions and high temperatures found in industrial cells. Earlier studies show that a water model can be a viable tool for observations on alumina feeding and dissolution, as presented in Chapter 3.

Several initial experiments are conducted to gain knowledge of how rafts are formed, and how to optimize the water model to increase its similarity to industrial cells. To perform a parametric study on alumina feeding and dissolution, a reproducible method for the experimental implementation needs to be developed. Furthermore, the overall objectives of this thesis can be summarized as:

- Facilitate conditions in which the water model provides good resemblance to an industrial cell.
- Ensure the best conditions for automated image analysis with high reproducibility.
- Investigate how variations in temperature, particle size, and gas evolution affects raft formations quantitatively.

Chapter 2 will go into detail on alumina feeding and dissolution, before Chapter 3 will review literature within physical model studies, including water models. Initial experiments, results and discussion will be presented in Chapter 4, before water model experiments are described in Chapter 5 with results following in Chapter 6. A final discussion is given in Chapter 7 before concluding remarks and further work are presented in Chapter 8.

2 Alumina in the Hall-Hèroult process

Alumina, (Al_2O_3), in the form of powder, is the raw material periodically fed into the electrolysis cell to produce aluminium during the Hall-Hèroult process. Quality of the alumina powder does not only affect the purity of the metal, but also the cell operation and the production itself [3, p.63].

Aluminium oxide is refined from bauxite, a sedimentary rock with a considerable amount of aluminous minerals, almost in its entirety using the Bayer process. This process is mainly divided into three steps; extraction, precipitation and calcination. Especially the calcination-step of the process, where an aluminium-hydroxide named gibbsite ($Al(OH)_3$) is transformed into alumina, is important for the properties of the oxide. In this heating process, structural changes in the mineral occurs and several different crystallographic phases of alumina takes form. Simplified, the crystallographic forms are referred to as γ-alumina, some metastable forms, and a calcination above a certain temperature (1250°C) enables a complete conversion to the stable α-alumina possible [3, p.63]. However, the final alumina product from the Bayer process usually consist of less than 10% of the thermodynamically stable α-phase [2]. In a review by Lavoie et. al. [6], it is pointed out that observations made in laboratory studies have shown that the α-alumina with its low surface area makes dissolution of the alumina fed slower. The rapid transition from γ-alumina to α-alumina is related to the formation of agglomerates when added to the bath [7]. This formation of alumina agglomerates is later described in detail in this chapter.

Specifications for alumina powder are many, including chemical purity and the amount of different phases. Several alumina properties are interrelated and properties like the surface area of the particles, flowability and particle size distribution (PSD) affects the dissolution rate of the powder in the bath [3, p.65-67] [8].

2.1 Particle size distribution (PSD) and fractions

PSD is ranked among the most essential properties of alumina. To be more specific, the content of small particles is of most importance when ranking the different alumina properties [3, p.74].

According to Kazás et al. [9], the shape of alumina particles is hard to describe, but is close to spherical, as seen in Figure 2.1, although it is porous and laced with edges.
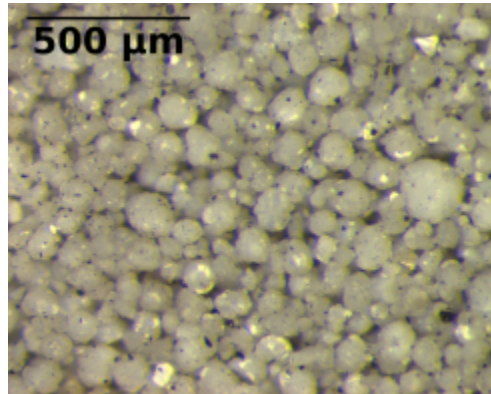
Figure 2.1: Light microscope image of alumina particles.
[10]

Alumina particles varies in size from approximately 20 μm to 150 μm, and are categorized into specific fractions. The "coarse" fraction is a percentage of particles retrained by a +100 μm screen with square section holes, while the "fine" fraction is a percentage of particles smaller than 45 μm. The smallest fraction of particles is called "superfine" and is the percentage of particles smaller than 20 μm. In the production process, the percentage of fractions used varies between different smelters, but there are some typical standards within the industry. The coarse fraction is usually less than 15% but can be significantly lower depending on the smelter. Typically, the fine fraction is less than 20% and the superfine fraction is limited to a maximum of 0.5% [3, p.66-67].

The alumina PSD is closely monitored, as too large or small particles may cause process complications. Larger particles are undesirable due to low solution rate in the bath, while small particles may increase dust emissions and possibly complicate mechanical handling [3, p.66].

2.2 Dry scrubbing

Before entering the cell, the alumina goes through a dry scrubbing process. This process is based upon the chemical reaction where emitted fluoride gases from the cell are absorbed by the alumina. The alumina emerging from the dry scrubbing is called secondary alumina or smelter grade alumina (SGA), and is the actual powder that is fed into the cell.

The dry scrubbing process benefits the aluminium production in several ways. Positive environmental effects are the utilization and capturing of dangerous fluoride gases, which otherwise would enter the air. Secondary alumina also contributes to the recycling of fluoride back into the cells, which are expensive to add otherwise [3, p.83]. Studies have additionally shown that the secondary alumina dissolves faster than primary alumina [11].

2.3 Alumina feeding and dissolution

The feeding of alumina to the bath is key in maintaining effective, high quality production of aluminium. Point feeders, introduced simultaneously by Pechiney and Alcoa in the 1970s, revolutionized aluminium production and is an essential component in modern cells [12]. This introduction contributed to streamlined production and reduced emissions. Implementation of point feeding technology allowed greater control of the cells through the regulation of feeding parameters such as quantity and time intervals. Regulating these parameters ensures continuous cell operation at optimal alumina saturation (2-3 wt%), which is important to promote stabilization of the bath and diminish disturbances in the crust [3, p.50] [13, p.855]. These contributions reduce energy consumption and increases production efficiency.

2.3.1 Anode effects

Alumina content in the bath outside the desired range causes unfortunate production disturbances like anode effects. For higher concentrations of alumina, excessive amounts of alumina sludge will be collected underneath the metal pad. This results in an undesirable disturbance of the current path which leads to unstable flow of the metal pad and other negative consequences [14]. Lower concentrations of alumina leads to an anode effect caused by an insulating layer formed underneath the anode. In advance of this anode effect, gas bubbles formed at the anode grows larger in size preventing

the electrolyte from wetting the anode. This insulating layer of bubbles will eventually cover all of the anode surface submerged in the bath, resulting in a rapid increase in cell voltage. This voltage increase causes the anode gas composition to change by producing CO and trace amounts of perfluorocarbon (PFC) gas compounds, mainly CF_4 and C_2F_6 [2, p.50] [3, p.210] [6]. These gases are harmful to the environment because of a high global warming potential and have therefore received considerable attention in recent years. The amount of these PFCs can be calculated to CO_2-equivalents, where 1 kg of CF_4 and C_2F_6 are equivalent to 1.7 and 12.2 metric tons of CO_2, respectively [15]. Point feeding has shown a remarkable lowering of these gases, including a reduction in PAH and PFC emissions by 90% [12].

2.3.2   Point feeding

Feeding of alumina to the bath is a simple, yet complicated process. Modern aluminium cells have point feeders strategically placed inside the cells. The basic principle of these feeders is shown in Figure 1.1 and consists of two steps: breaking the crust and feeding alumina. Some point feeder designs combine these two steps into one single execution. Breaking the crust is done with piercing rods driven by pneumatic cylinders. These rods puncture the crust and leaves holes with diameters from 6-10 cm. The alumina is fed to the bath through these holes in doses that typically varies from 1 to 5 kg per cycle [6]. Point feeders are operating at two to six spots in the cells, typically evenly distributed between anodes in the centre channel, repeatedly adding alumina to the bath [13, p.864]. For example, a 300 kA cell will have a dose of 1 kg added every 20 seconds on average [3, p.79-82][1, p.46]. The point feeders are activated by computer controlled systems with sophisticated algorithms that seeks to keep a satisfactory alumina content in the electrolyte [13, p.864]. It is crucial that the small amounts of alumina added is quickly dissolved and mixed with the electrolyte. Therefore, a well dispersed feeding is needed to ensure a continuous concentration of alumina in the bath, which will provide stable operational conditions facilitating effective aluminium production [3, p.50]. This avoids formation of sludge and greenhouse gases, further emphasizing the significance of optimized feeding in the production process.
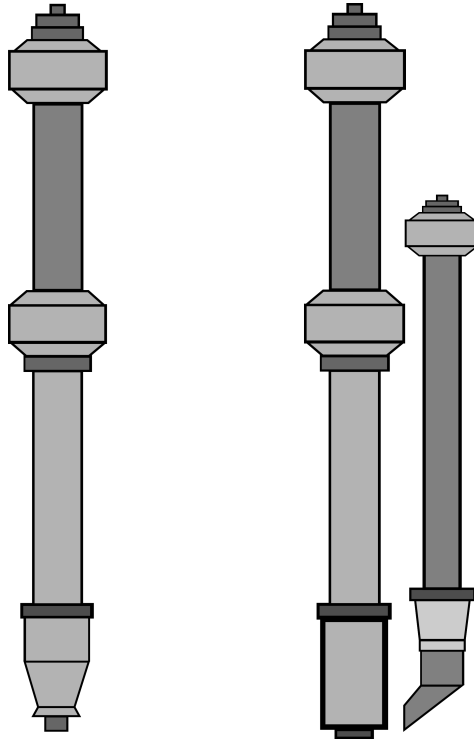
Figure 2.2: Integrated (left) and independent (right) feeders.
[16, p.20].

There are two base designs of point feeders as shown in Figure 2.2. The integrated feeders uses one cylinder which combines both crustbreaking and feeding into a single action. This design functions by using high speeds to instantly break the crust and subsequently feed a dose of alumina while the feeder is still in the hole. Most of the alumina will fall into the bath as the feeder returns to its original position. Some remaining alumina will create a buildup along the edge of the feeding-hole, creating a volcano shape around the hole [16]. Alumina buildup and crust formation can affect the feeder hole condition by causing difficulties with crustbreaking. Feeding into closed holes may force the breaker to push the alumina through the solid crust to be able to reach the bath. This is a phenomenon referred to as a "push feed" by Lavoie et al. [6]. Feeder hole condition typically worsens over time, often increasing the amount of "push feeds". These contribute to limiting the dispersion and slowing dissolution, in addition to possibly causing formation of sludge.

The independent feeders uses separate cylinders for crustbreaking and feeding. This introduces the opportunity to have multiple feeding-cycles (2-3) with only breaking the crust once [16, p.24]. This will significantly decrease the number of breaking-cycles,

which in turn contributes to lower maintenance costs and reduced energy consumption. Therefore, the lifespan for independent feeders is typically 5-6 years versus 1-4 years for integrated feeders. However, capital costs for these feeders in a 300 kA cell will be about 30 000 USD and 10 000 USD respectively [16, p.28]. It is advantageous to have a reliable feeder that performs well over a long time, opposed to short-lived feeders with malfunctions and failures. This may be a contributing factor to the rise in use of independent feeders.

Replenishing the electrolyte properly is imperative in maintaining ideal operational conditions. According to a review by Lavoie et al. [6] there are three important steps required in order to ensure proper addition and dispersion of alumina. These fundamental dissolution factors seeks alumina to be:

1. Reliably delivered in sufficient quantity to the liquid bath.

2. Dispersed in the feeding zone and dissolved rapidly within the electrolyte.

3. Distributed under all the anodes in the cell to exceed a minimum concentration to avoid anode effects.

Alumina should preferably be fed to the bath as homogeneous particles without any formation of agglomerates. This is important for optimal dispersion and assures rapid dissolving. Optimal dispersion prevents accumulation of powder, which in turn may lead to formation of rafts and/or sludge. These agglomerates are a natural consequence of the feeding process. Although it is more apparent through conventional feeding, it is hard to avoid completely and therefore still present to a certain degree even with point feeding technology [6].

2.4 Dissolution of alumina

Dissolution of alumina powder in the cryolitic bath has been studied for decades. Even with the fairly high solubility of alumina in such melt ($\sim$10 wt%), alumina dissolution in the cell has always been a major concern in process operation [17]. With the increase in both cell sizes and electrolysis intensity, the dissolution has become harder to control, thus increasing the importance of an efficient alumina feeding and dissolution [6].

After the initial feeding and dispersion of alumina into the cryolite, a portion of the powder will stay afloat on the surface of the molten bath. This is a well-known phenomenon observed both in the industry and in experimental research projects, hindering

dispersion and direct contact between much of the powder and the bath, thus delaying dissolution [18]. Kaszás et al. [18] states that this floating-phenomenon and its effects have not been properly researched, and that the main body of research on this topic mostly focus on determining and modeling the dissolution rate of alumina, in addition to the different mechanisms driving the dissolution [19] [17].

When the alumina ($\sim$150-200°C before injection) is added to the electrolysis cell ($\sim$955-965°C) and contact between the introduced powder and the bath occurs, a frozen layer is typically formed around the particle surface due to the temperature difference. Alumina-particles in close proximity can freeze into larger flakes and these particle-groupings are known as agglomerates. They can partly be surrounded by bath, creating a floating raft on the bath surface with alumina powder on top of the raft [10]. The formation of rafts, these slow-dissolving agglomerates, is unfortunate for the overall dissolution and may potentially lead to anode effects. Rafts could occasionally, due to the higher density of the agglomerates, sink down to the metal pad, and eventually form sludge if sinking all the way to the bottom of the cell. Sludge is, as formerly mentioned, undesirable as it can have a negative effect on the cell operation [20]. By investigating the structure of the rafts, it has been established that they consist of three different layers. The layers are divided into solidified bath, alumina infiltrated by the bath with changing composition and dry alumina. Additionally, infiltrated alumina has been found in pores in the layers of frozen bath [18].

In a review describing alumina feeding and dissolution factors, Lavoie et al. [6] presents a four-step process for the dissolution itself. This process is described below and in Figure 2.3.

1. The alumina is fed to the cell and hits the bath surface. Alumina particles which are well dispersed will dissolve quickly into the electrolyte.

2. The big leap in temperature between the cold alumina and the molten bath results in a frozen layer of electrolyte (cryolite) being formed around the surface of particles. Several alumina-particles in proximity could clump together and form rafts or agglomerates.

3. The layer of frozen electrolyte must melt before further dissolution of the alumina. The melting of the frozen bath is heat transfer controlled.

4. With the layer of frozen electrolyte melted down, contact between powder and the liquid bath is re-established and dissolution of alumina can continue.

It is pointed out that with a lack of heat, steps 2-3 could possibly be repeated since the dissolution itself is an endothermic reaction [6].
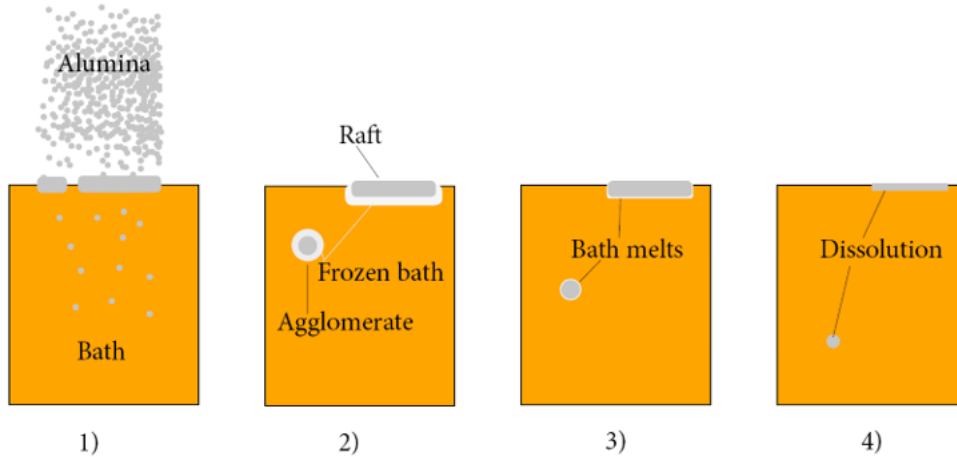
Figure 2.3: Illustration of the four-step process depicting alumina feeding and dissolution described by Lavoie et al. [6].
[10]

The first step describes a rapid dissolution, while a slow dissolution occurs in the next three steps. This is clearly illustrated in earlier work regarding dissolution rate [19] [17]. Figure 2.4 shows a dissolution curve from Haverkamp and Welch [19], where dissolved alumina is measured as a function of time. The curve can be divided into two main parts, with the first part depicting the rapid dissolution from well dispersed alumina. The second part shows the slower dissolution of the alumina agglomerates.
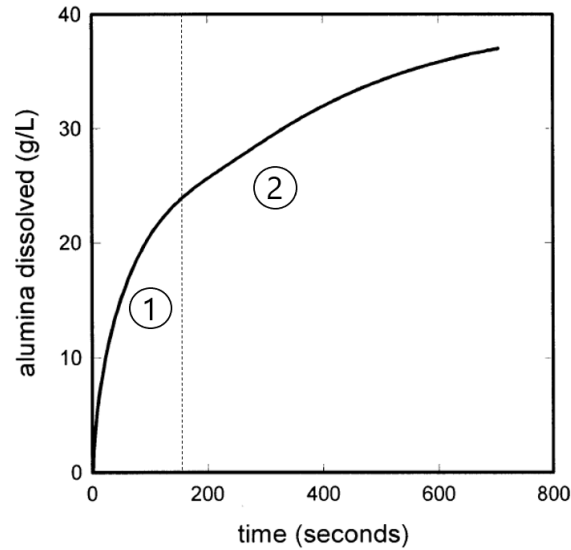
Figure 2.4: A dissolution curve measured by Haverkamp and Welch [19]. The curve can roughly be divided into two parts, demonstrating the different stages in the dissolution process. 1) Rapid dissolution of well dispersed alumina. 2) Slower dissolution of alumina agglomerates and rafts.

Gylver et al. [21] points out that the formation, floating and break-up of the rafts are determined by macroscopic properties, such as size and density. These characteristics are in turn related to for example the interconnection between grains and other microscopic properties. Another study by Gylver [22] investigated the relations between raft behavior and cell conditions. During this study it was observed and recorded that floating time varied considerably, between 5 and 140 seconds. Some of the rafts sank immediately after feeding, while some remained afloat until the subsequent feeding.

In an industrial cell, gas bubbles from the anodes have been observed to give a splashing effect which contributed to the dissolution of the dispersed alumina [22]. The bath would splash on the floating rafts and help to consume and dissolute the alumina from the sides. The release of anodic gases and its contribution to the alumina dissolution are also pointed out using physical laboratory models. Chesonis and LaCamera [23] used such a model and stated that the pulsing of gas bubbles into the anode gap created an oscillating effect in the bath which facilitated both dispersion and dissolution.

The dissolution of alumina in the cryolite bath is a complex process where mass and heat transfer, phase transition and agglomerate formation are coupled at the same time

[24]. Different mathematical models trying to describe the raft formation and alumina agglomerate behavior have been developed to further increase the knowledge regarding these phenomena [25] [24]. Thus aiming to improve the alumina feeding and dissolution in the aluminium production to secure both a more efficient and secure process.

3   Review of water model experiments

The high temperatures (~ 960°C) in an industrial aluminium reduction cell and the corrosive nature of cryolite at these temperatures makes direct measurements in a cell difficult. This aggressive environment is challenging and affects both observations and recordings in the industry. Physical models, mostly in room temperature, have of this reason often been used to simulate and describe different phenomena in the aluminium process. The extensive use of physical models during the last decades has to a large extent, as stated by Einarsrud [26], been used to validate computational models related to the bath flow. Studies on the gas induced circulations related to gas release from the anodes have been prominent.

Cooksey and Yang [27] used a full-scale air-water model with three anodes to study bubble behavior and gas-induced liquid flow. Moreover, they listed several studies that have applied physical models in the research of different phenomena that occurs in the reduction cell. This included studies of bubble-flow patterns, bath/metal interface motion and alumina distribution. It was noted that the use of a single anode or half-anode, as used in most of the mentioned studies, is considered a significant simplification [27].

A wide range of different physical models have been used in studies throughout the years. Traditionally, a two-fluid system in a water-oil model has been used, where water and oil simulates the bath and metal layer. Studies regarding deformations of the bath-metal interface are made possible with such a model. When the cathode is simulated as a fixed boundary, as in the model used by Fortin et al. [28], studies of such phenomena are not possible.

Full-scale models with multiple anodes have also been used [23] [28]. Chesonis and LaCamera [23] used their full-scale model to study how the alumina distribution and interface motion was affected by the gas-driven circulation in the cell, especially from anode gas evolution. Circulations patterns were estimated using computers, and used to simulate flow fields caused by Lorentz forces in an industrial cell. Additionally, the model was used to study alumina distribution and dissolution. Results indicated that the gas-driven flow had a bigger influence on the alumina fed than the electromagnetic flow and was a significant contributor to the dissolution of alumina.

Chesonis and LaCamera [23] further observed that the pulsing of gas bubbles created oscillation in the bath flow, which in turn facilitated both distribution and dissolution. Furthermore, the study addressed how variations in current density affected the time required to distribute the alumina feed in the bath with the combined gas-driven and electromagnetic bath flow, shown in Figure 3.1. The graph shows a reduction in the time required to distribute the alumina feed with increased current density. In another full-scale study by Fortin et al. [28], focusing on the effects of variations of the cell operation conditions upon the anode gas behavior, variation in current density was one effect investigated. The change in this variable was simulated with variations in the air flow rate, and a "strict" correlation between the current density and the gas flow rate was pointed out. The size of gas bubbles released from the anode and the gas bubble velocity were observed to increase with the current density (gas flow rate).
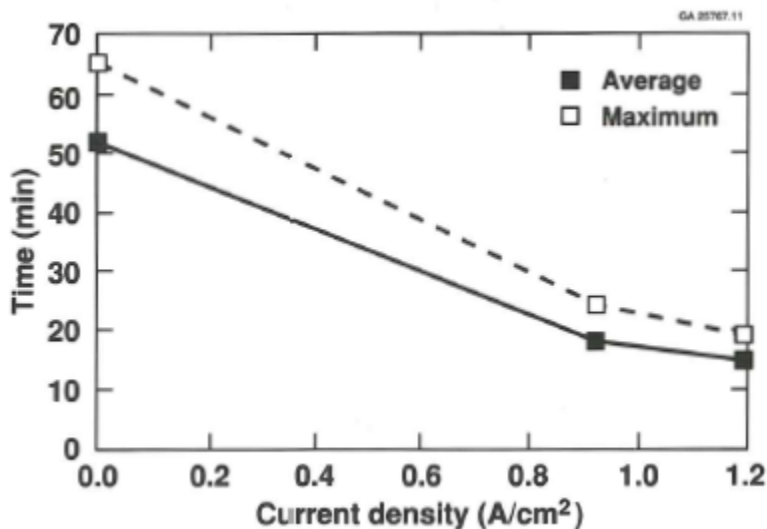
Figure 3.1: Graph showing feed distribution time plotted against anode current density, from a study of Chesonis and LaCamera [23].

Recently, Gylver [10] carried out some "cold experiments" where addition of alumina to a liquid was studied. The aim of the experiments was to see if any predictions regarding alumina behavior when added to molten cryolite, such as dispersion and floating, was possible. Different heights and feeding methods were tested to see what would serve best for further laboratory testing. In this experiment, two types of liquid were used, clean water and saline water.

As initially mentioned, physical models have mostly been used to validate computational models related to the bath flow. However, Roger et al. [24] recently presented the development of a mathematical model to simulate raft formation, where water model experiments were used to validate the model. These experiments consisted of a funnel-injection of organic particles (10 g), pre-cooled to around -180°C with liquid nitrogen, into static room tempered water (20°C). A high-speed camera was used to document the experiments in a transparent water tank and to compare the results with computer simulations.

Similarities in the shape of rafts were found between the experimental results and the computer simulations, and when the injection method changed, the form of the raft changed accordingly. Additionally, rafts with the likeness of those recovered from laboratory and industrial cells were observed from images [22]. This study by Roger et al. [24] concluded that the mathematical model had the potential to simulate and improve alumina injection.

4 Initial experiments

Initial work and experiments were performed to facilitate the main experiments in the water model and are described in the following chapter. An industrial visit at Alcoa Mosjøen both influenced optimization work on the water model and the search for a applicable powder determination. The powder determination resulted in an analysis of the PSD in addition to tests focusing on finding a suitable crushing procedure for the powder in the coarse batch.

4.1 Visiting Alcoa Mosjøen

A trip to aluminium smelter Alcoa Mosjøen was conducted during this project to improve the understanding of the aluminium production process. In collaboration with SFI Metal Production, where Alcoa is a partner, an exclusive tour around the plant was given to provide insight in the aluminium production process.

During the tour around the plant, a cell line was partly opened with removal of crust near a feeder hole to show how alumina feeding and dissolution were performed. Observations and recordings were done for comparison to feeding and dissolution later performed in the water model.

Experimental setup

The setup for recordings of the industrial cell was quite simple, only including a Sony Cybershot DSC-RX10 IV camera and a tripod. However, the camera was negatively affected by the strong magnetic fields present at the plant, which caused it to malfunction. To avoid these effects, another cell had to be used as the initial position was between cell lines. A cell along the outer wall of the plant was found more suitable, and a new hole in the crust was quickly created. Furthermore, the camera was moved away from the cells when powering on and adjusting the focus. The camera was then carefully returned to the recording position while keeping as much distance to the cells as possible. It was then placed on the tripod with a height of about 1.5 m and distance to the cell set to approximately 5 m. This exact placement was used for recording multiple feedings in the cell.

Results

The recordings were studied afterwards, with one of the recordings having sufficient focus and quality to be of further use. Sample images from this recording are shown in Figure 4.1 and were used to compare the visuals of raft formation and dissolution in industrial cells to the water model. Rafts are depicted in the centre of the images as an elongated dark strip in the glowing cryolite bath. The crust is shown along the side edge and the rafts are observed through the feeder hole of this insulating layer.
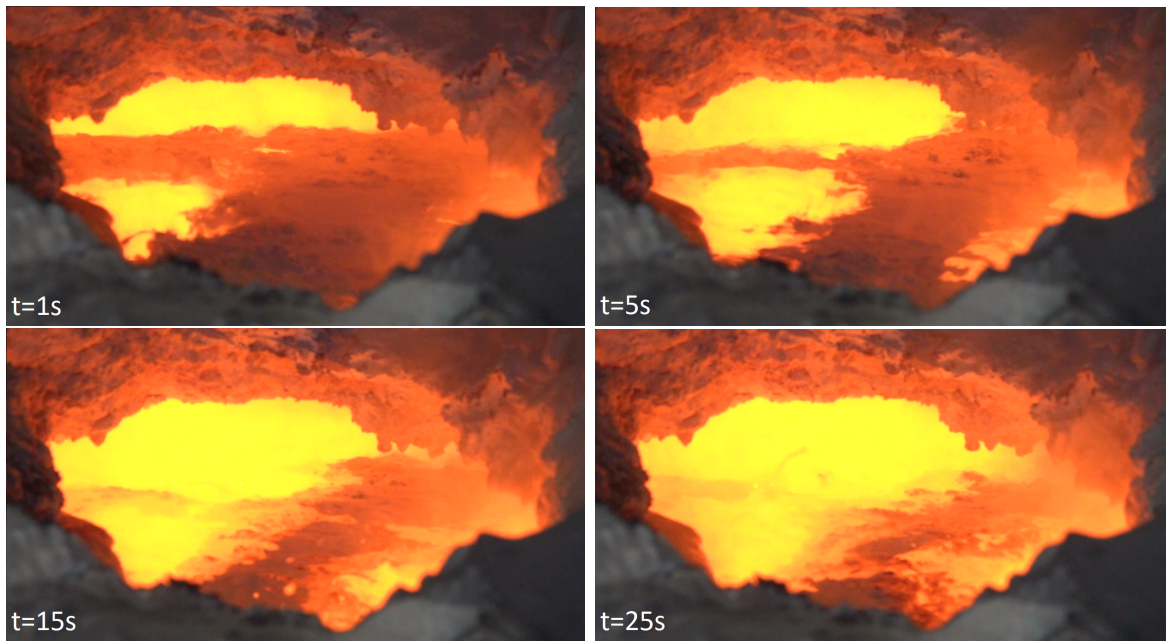
Figure 4.1: Sample images of raft formation and dissolution after feeding of alumina in an industrial cell (Alcoa Mosjøen) at selected time intervals, video available at (`https://youtu.be/KooLOmzL5VO`).

4.2 Powder determination

Observations of feeding and dissolution performed in the water model required a type of powder to simulate alumina. Some requirements were set for the powder to be used, as it needed to:

- Form rafts when frozen and dispersed into cold water.

- Dissolve in water without discoloring it.

- Dissolve in water without forming foam or other disturbances that disrupts recordings or image processing.

Experimental setup

Different types of organic powders were tested in small-scale attempts, performed in a large beaker (diameter: 18.5 cm, beaker-height: 27 cm, water height: 5.5 cm) with similar conditions as the water model. The powders tested were cooled down in an ultra-freezer to around -80°C while water, used as bath, was cooled down to near the freezing point. Small samples of different powders, listed in Table 4.1, were added to the water by hand from an approximate height of 22 cm above the water surface. All attempts were recorded from the side with a Canon PowerShot G12 camera.

Observations regarding the rafts resemblance to alumina feeding and dissolution was rated to select which powders should be further tested in the water model. From the nine powders tested, three were selected for large-scale testing.

Table 4.1: Powders investigated in small-scale testing.

Number	Powder
1	Almond flour
2	Potato flour
3	Icing sugar (Fresh)
4	Cornflour
5	Bake protein
6	Coconut flour
7	Creatine
8	Vanilla sugar
9	Natreen sprinkle sugar (hand-crushed)

Powders excluded from large-scale testing in the water model had inconvenient characteristics when dispersed into water. Some powders did not dissolve, sinking to the bottom in large chunks. Other powders discolored the water or had an incomparable behaviour to alumina dispersion.

Preparatory work with the model used icing sugar to simulate alumina feeding and dissolution. This powder was further tested in the water model with various processing methods done in advance, along with the selected powders from small-scale testing. A total of eight different powders and combinations were tested in the model, listed in Table 4.2.

Table 4.2: Powders investigated in the water model.

Number	Powder
1	Icing sugar (Stored)
2	Icing sugar (Heated to remove excess water)
3	Icing sugar (Fresh)
4	Icing sugar (Stored) mixed with gelatin 50/50
5	Vanilla sugar
6	Natreen sprinkle sugar (Hand-crushed)
7	Maltodextrine
8	Sukrin icing sugar

Results

The powder that resembles the most with alumina feeding and dissolution in an industrial cell is an artificial sweetener by the brand Natreen (sprinkle sugar), mainly consisting of maltodextrin and aspartame.

When Natreen is crushed into smaller fractions and frozen it tends to form rafts on top of a cooled water surface in the same way alumina powder does in cryolite melts. It dissolves in the water at a reasonable rate for observations, without discoloring it too much or disturbing the recording from above.
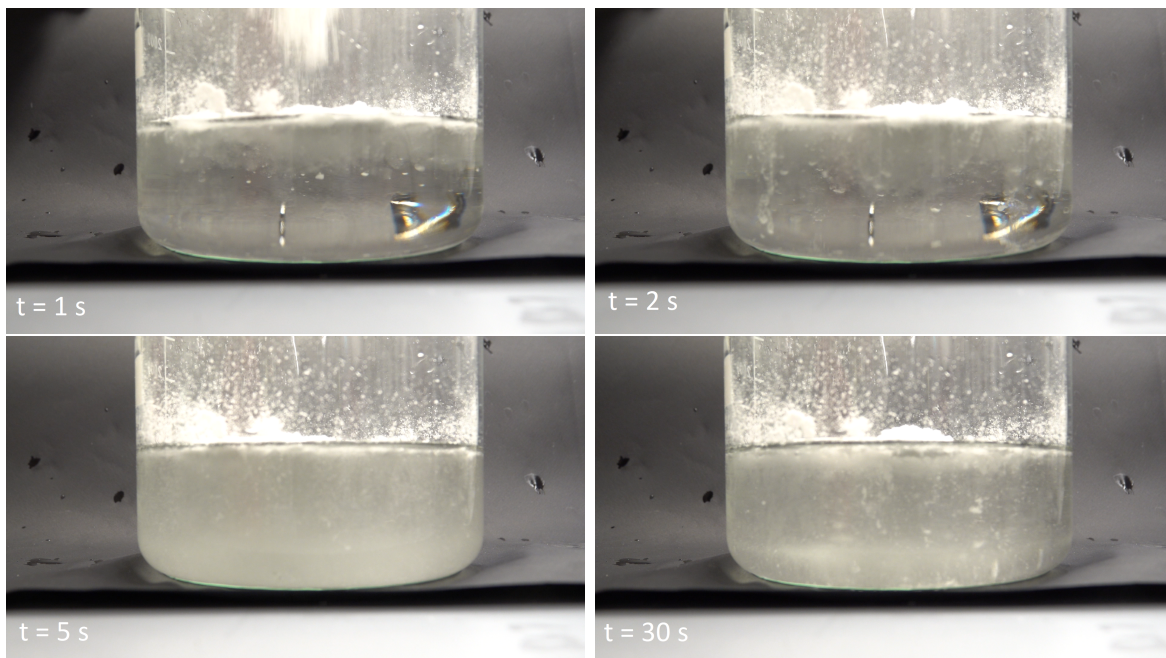
Figure 4.2: Images of small-scale testing with hand-crushed frozen Natreen dispersed in cooled water at selected times.

Figure 4.3 displays raft formation and dissolution of Natreen from recordings in the water model. Both dispersion and raft behavior resemble the industrial rafts shown in Figure 4.1. The powder is initially widely dispersed and forms elongated rafts across the surface. These rafts narrows and spreads over time, before eventually fully dissolving in the bath.
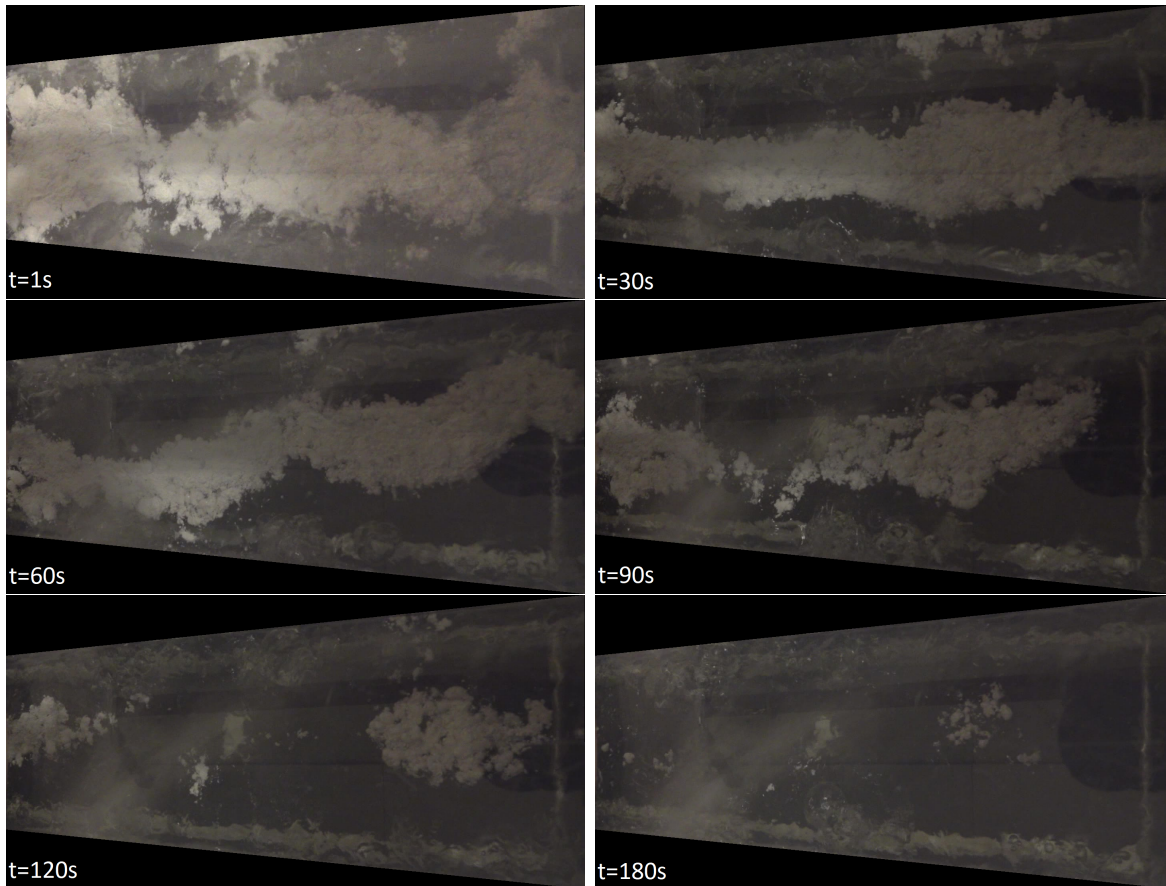
Figure 4.3: Sample images of raft formation and dissolution after feeding of Natreen in the water model at selected time intervals.

4.3   ImageJ

ImageJ is a Java-based open-source image processing tool. In 1997 its development was started by Wayne Rasband who already had developed similar imaging programs. He worked at the National Institutes of Health (NIH) and even though he retired in 2010, he continues to develop the software [29]. ImageJ has extensive image processing properties with its recordable macros and Java plugins. This introduces possibilities to develop necessary plugins, as well as extended opportunities in automation of complicated image analysis.

4.4   Particle size distribution

The PSD of Natreen powder used in this study was measured using a scanning electron microscope (SEM) and image analyzing measurements in ImageJ. Data was further treated and displayed using Microsoft Excel [30].

Before examination in SEM the powder went through a specific treatment. The first step of the treatment was to heat up the powder in an oven to remove excess water. A small sample of powder was placed on a specimen of aluminium with double sided adhesive carbon tape. The specimen was then placed in a container where it was sputter-coated with a gold-layer to provide a conductive surface. Images taken in SEM was further treated in ImageJ [31].

The scale-bar retrieved in every SEM-image was used to determine the number of pixels per unit of measurement. This was important for further analysis when measuring the area of each particle. ImageJ has a built-in module for particle analysis. When analyzing an image, the range of particle size was set by determining the smallest and biggest particles to be measured. Usually the range of the smallest particles varied between 10 μm and 30 μm, given satisfactory quality of the image. Poor image quality may lead to disturbance of the analysis by splitting a particle into several pieces and counting the same particle multiple times in smaller fractions. No upper limits were set.

To ensure sufficient image quality, brightness, contrast, and threshold were adjusted manually in each image before the particle analyzer measure and lists the results, as shown in Figure 4.4. To measure the size of the smallest particles present, at least three images were taken to obtain smaller particles attached to single grains as seen in Figure 4.5. During this analysis the range of particle sizes were set from 0.9 μm. The particle

analyzer generated a new image with outlines of each particle measured, as displayed in Figure 4.6. In addition, a table was generated where area of each particle was listed. For every powder analysed, no less than 10 images in total were processed in ImageJ.

Slice	Count	Total Area	Average Size	%Area	Mean	Median
sbl20200310.004818_tresh.jpg	54	18978.912	351.461	6.811	255	255

	Area[μm^2]	Mean	StdDev	Median	XStart	YStart	Diameter [μm]
1	146,939	255	0	255	716	23	13,678
2	2393,197	255	0	255	949	67	55,201
3	1295,465	255	0	255	567	123	40,613
4	123,129	255	0	255	1025	162	12,521
5	1363,265	255	0	255	740	249	41,662
6	503,628	255	0	255	400	282	25,323
7	34,921	255	0	255	1064	283	6,668
8	903,855	255	0	255	556	293	33,924
9	959,637	255	0	255	304	297	34,955
10	531,066	255	0	255	1089	299	26,003
11	502,494	255	0	255	446	306	25,294
12	32,88	255	0	255	1068	309	6,470
13	1969,161	255	0	255	448	367	50,072
14	21,088	255	0	255	429	390	5,182
15	1122,676	255	0	255	846	400	37,808
16	74,603	255	0	255	549	401	9,746
17	36,508	255	0	255	426	420	6,818

Figure 4.4: Example of an image treatment from SEM during a particle size analysis performed in ImageJ. The SEM image was taken with a magnitude of x200 and a scale bar of 100 μm. Threshold-setting and the outlines of the particles measured were shown, before the measured area was generated and listed.

28
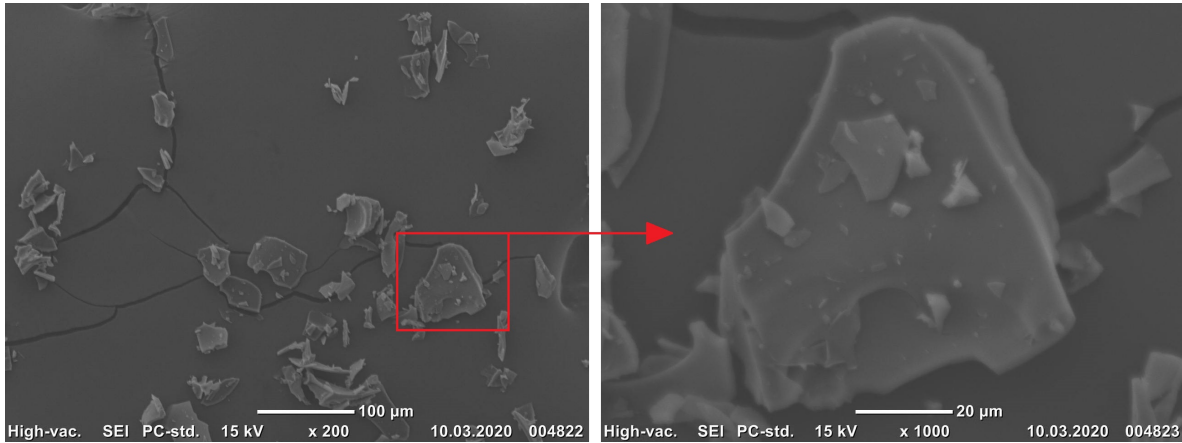
Figure 4.5: SEM image of Natreen, focused on a single grain for measurement of the smallest particles present. The images were taken with a magnitude of x200 to the left and x1000 to the right, with a scale bar of 100 µm and 20 µm, respectively.
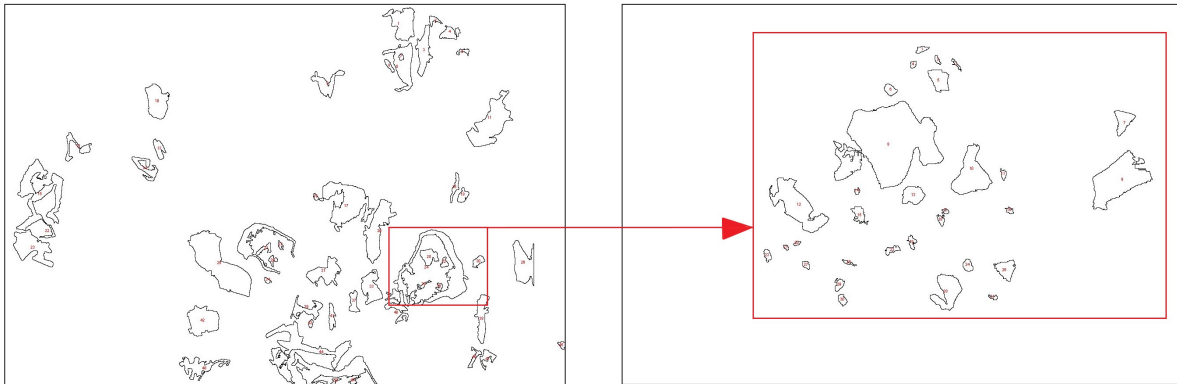
Figure 4.6: An image with the outlines of the particles present in Figure 4.5.

Further treatment of data was done in Microsoft Excel. The particle diameter was estimated based on the equivalent diameter of a circle.

$$d = \sqrt{\frac{4A_p}{\pi}} \tag{4.1}$$

Where A_p is the area of the particle measured in ImageJ, and d is the diameter. From the diameter calculated, a table with the frequency of different particle size intervals was created using the "Data analysis" tool in Excel.

This table was further used to generate a cumulative distribution of the particles, which was used to determine the D_{25}, D_{50} and D_{75} values, i.e. the diameter of the particles present at 25%, 50% and 75% of the batch, respectively.

4.5   Crushing procedures

Natreen powder used to simulate alumina needed to be crushed into smaller fractions before conducting experiments. Originally, Natreen has a rather porous structure, and needs to be crushed into smaller fractions to give the desired effect. This provided the opportunity to choose controlled particle size as a measurable parameter in water model experiments.

Experimental setup

Due to Covid-19, laboratory access was restricted, making PSD challenging to control when crushing powder. The first batch of powder (the fine batch) was crushed at home while other test procedures were performed at the laboratory. The same method of powder crushing was conducted for the same batch, while PSD was determined subsequently. Investigations were done to determine a crushing procedure for the coarse batch.

Images of the powder were taken in SEM for all test procedures as described in Section 4.4 for determination of PSD.

Powders were crushed in a Wilfa SL-1200W blender. The crushing procedure consisted of alternately turning the blender on and off in limited time intervals for several cycles. This ensured that the powder was crushed by the knives in the bottom of the blender, rather than floating around in the blender container. The blender was power regulated and three different settings were used in the crushing procedure: low, medium, and high. Whereas "low" was the lowest possible power setting provided by the blender, "high" was maximum power, and "medium" was a setting between the two.

Results

The results of the investigations in determining a crushing procedure for the coarse batch are listed in Table 4.3 and shown in Figure 4.8. The hand-crushed PSD is used as a reference, and the fine batch is also present to show the differences in PSD to be used in water model experiments. Crushed powder used in water model experiments are listed in Table 4.4 and displayed in Figure 4.9.

An image of crushed and uncrushed Natreen is seen in Figure 4.7 to display the differences in shape and size before and after crushing.
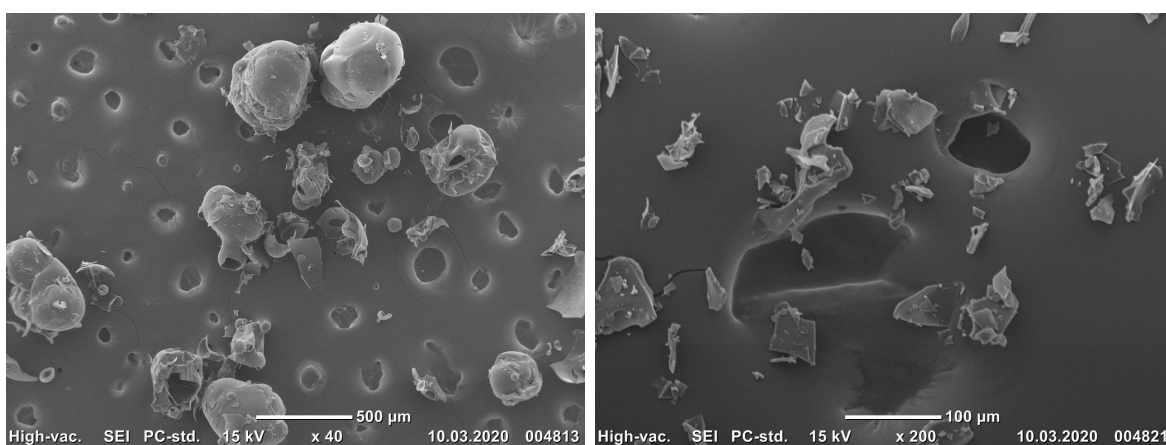
Figure 4.7: Images of unprocessed Natreen sprinkle sugar to the left with x40 magnification and a scale bar of 500 μm. Hand-crushed Natreen is seen to the right with x200 magnification and a scale bar of 100 μm.

The crushing methods used for the fine fraction and different procedures (P1-P4) tested for the coarse fraction are listed in Table 4.3, and the cumulative distribution in Figure 4.8.

Table 4.3: Crushing procedure and cumulative PSD for the hand crushed batch, fine batch and the four test procedures for determining the coarse batch.

Sample	Amount [L]	Power	Time interval [sec]	Number of cycles [#]	D_{25} [μm]	D_{50} [μm]
Hand crushed (Reference value)	1	-	-	-	6.5	13
Fine batch	2	High	5	5	6	10
P1	1	Low	2	2	9	16
P2	1	Low	3	3	7	13
P3	1	Med	2	3	5.5	8
P4	1	High	1	5	6	10.5
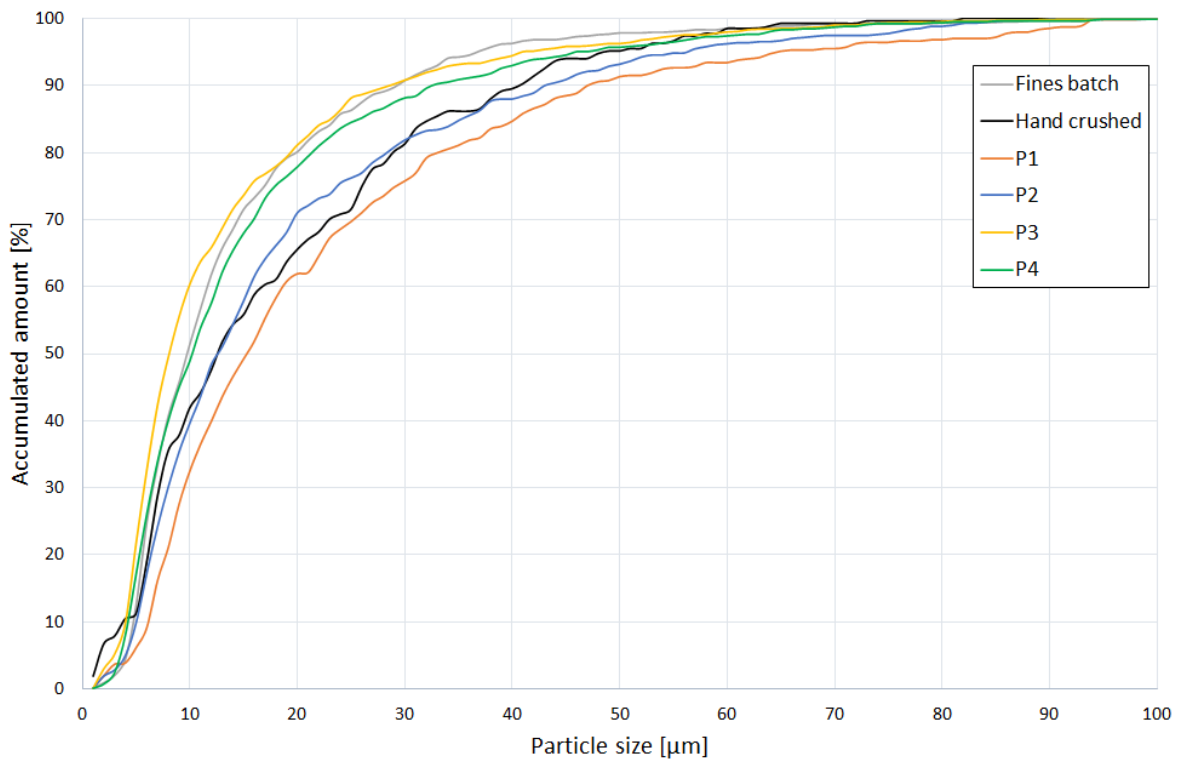
Figure 4.8: Cumulative distribution of the hand crushed batch, fine batch and the four test procedures for the coarse batch determination listed in Table 4.3.

The PSD for the coarse and fine batch used in the water model experiments are listed in Table 4.4 and Figure 4.9. Crushing method P2 was selected for the coarse batch.

Table 4.4: Differences in fine and coarse batch. D_{25}, D_{50} and D_{75} are the cumulative diameter at 25%, 50% and 75% seen in Figure 4.9.

Cumulative diameter	Fine [μm]	Coarse [μm]
D_{25}	6	9
D_{50}	10	17
D_{75}	17	29
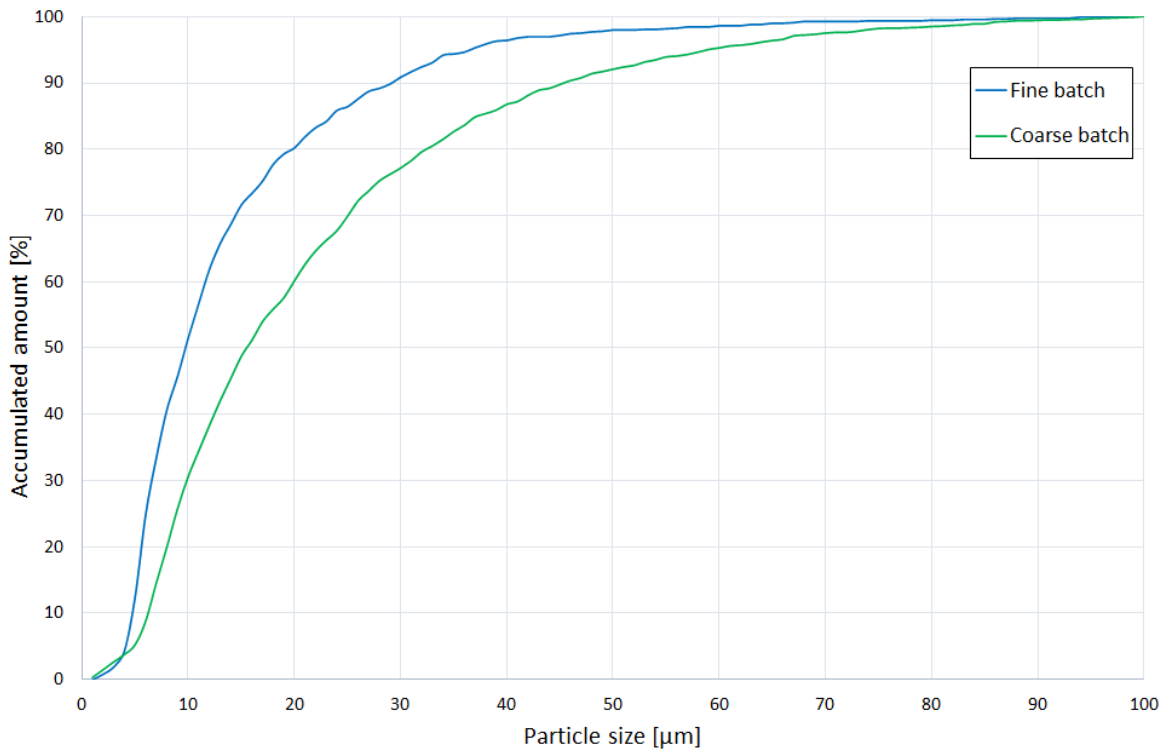
Figure 4.9: Cumulative distribution chart for fine and coarse batch used in water model experiments. The chart displays accumulated amount of particles in each batch where 25%, 50% and 75% are listed in Table 4.4.

4.6 Water model

The water model built for this project represents the cross section of the center channel in an industrial aluminium electrolysis cell, illustrated in Figure 4.10.
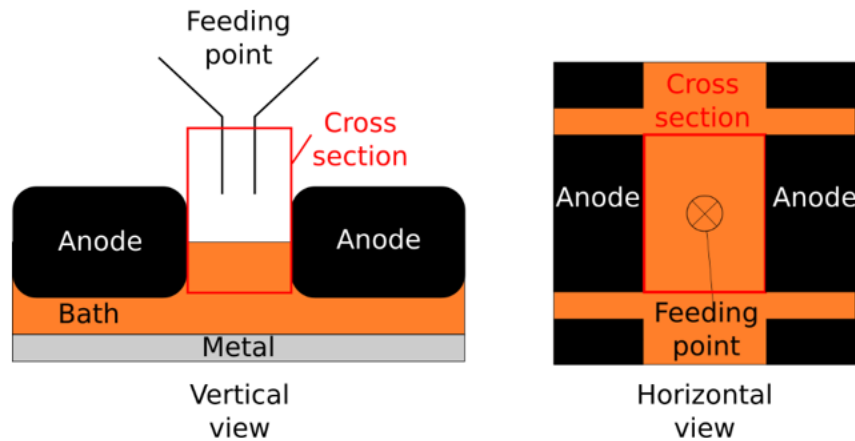
Figure 4.10: Illustration of the industrial cross section represented in the water model. The feeding point is placed between two anodes, in the middle of the anode gap.

[32]

The model had been optimized throughout the project, described in detail in Section 4.6.2, to reach the sought standards for the experimental tests. The original water model for this project is shown in Figure 4.11.
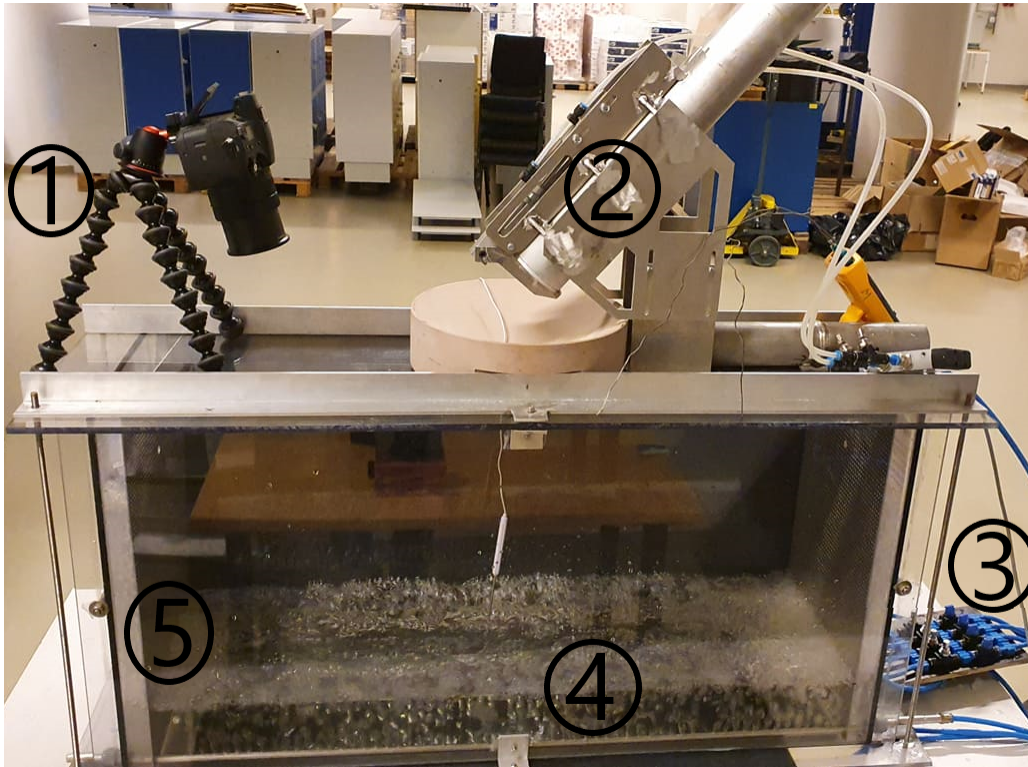
Figure 4.11: The water model before optimization. 1) Camera 2) Feeder 3) Gas-flow regulating panel 4) Bath with small bubbles generated from the two anode tubes at the long sides and the two convection tubes at the short ends 5) Ice chambers.

The dimensions of the model are presented in Figure 4.12, where the cross section has the same dimensions as the center channel of an industrial cell (width: 30 cm, length: 100 cm). The width of 30 cm represents the anode gap [26]. Gas from the anode tubes were introduced from bubble holes that covered around 90 cm of the model tank length since no bubble holes were situated in the ice chambers. The water tank was filled with the same 10.5 cm bath-depth in each test. With a water line at 10.5 cm, the distance between the feeder hole and the bath surface was around 50 cm.
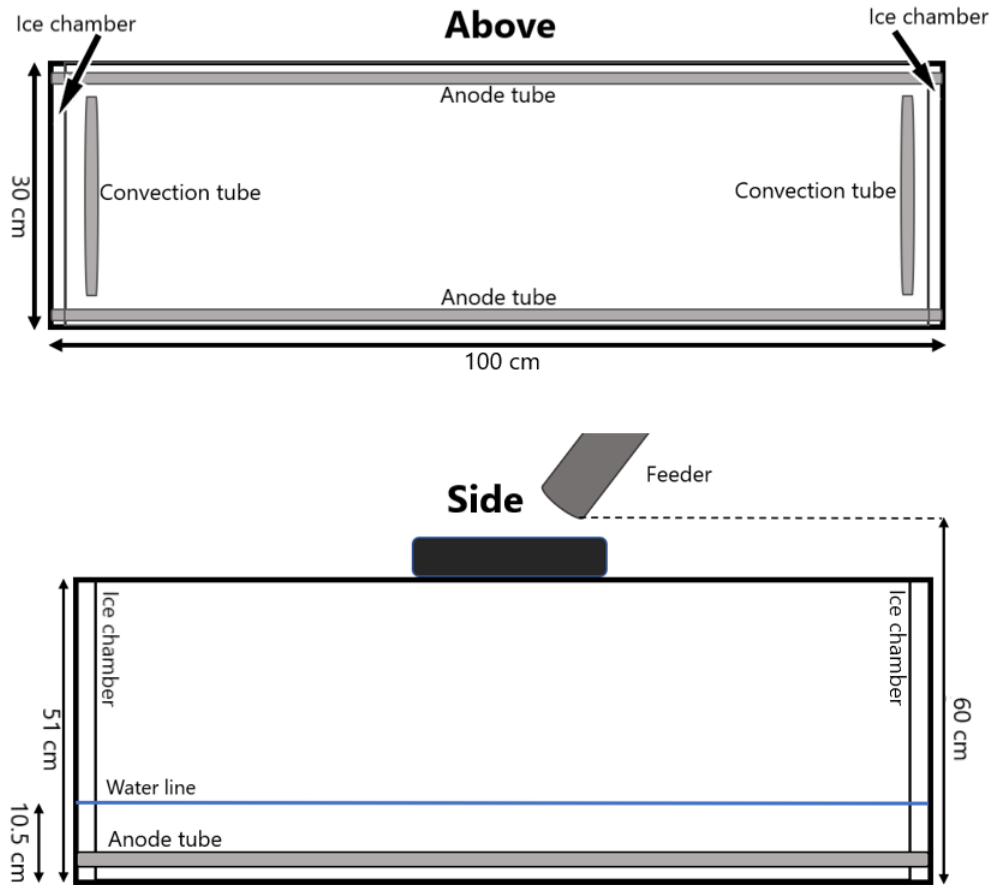
Figure 4.12: Schematics of the water model with its dimensions.

As Gylver [10] states, it is difficult to find a liquid at room temperature with the same properties as cryolite, shown in Table 4.5. For the experiments carried out in this model, water represented the cryolitic bath and an organic powder (Natreen) represented the alumina powder. Both the Natreen powder and the water was significantly cooled down to provoke a rapid freezing effect.

Table 4.5: Physical properties of clean water and cryolite [10].

Liquid	Surface tension	Density	Viscosity
-	[mN/m]	[kg/m³]	[mm²/s]
Water	72.8	998.8	1.003
Cryolite	140	2100	1.30

4.6.1 Description of the water model

The water tank was made of plexiglas and enabled visual observations and recordings of the experiments. The plexiglas plate at the bottom of the model worked as a fixed, rigid "cathode". A Sony Cybershot DSC-RX10 IV camera was used to document the experiments, and placed on top of the model to record the powder on the bath surface from above. A more thorough description of the remaining parts of the setup is listed below.

Feeder

Before entering the cell, the powder was placed in a feeder above the cell. The feeder was compressed air-driven and controlled by an electrical switch. The feeding technology replicated an independent feeder with an inclined feeding tube, based on Pechiney technology. It was situated in a fashion which ensured that feeding took place in the middle of the anode gap.

Bubble producing tubes

There was two different sets of tubes installed along the sides at the bottom of the model, see Figure 4.12. Anode tubes were located along the long sides to simulate the bubble formation at the anodes. As seen from Figure 4.10, the anode tubes simulate the short side of the industrial anodes, pointing towards the center channel. Convection tubes at the short ends could be used to simulate the longitudinal convection in the cell, however these were not used during experiments. From a panel attached to the tubes, each of the four tubes could be controlled individually. This included an on/off button and the possibility to adjust the gas flow.

The gas flow rate determined the bubble frequency and this parameter could be calculated and controlled with the use of Faraday's law and the ideal gas law for a specified current density [23] [28]. Flow rates of up to 200 L/min were used in the current work, with an example given in Appendix A.

Ice chambers

To maintain a desirable low bath temperature, near the freezing point of water, ice could be placed in insulated chambers situated at both short ends of the model, close to the inner wall.

4.6.2 Model optimization

In the work with optimization of the water model and the experimental setup as a whole, two main objectives were set:

- To improve the reproducibility of tests done in the water model and facilitate for an automated image analysis.

- To increase the realism of the water model to make it appear more similar to an industrial cell in its behavior.

Firstly, to improve the reproducibility of the model, the camera conditions were considered. Conditions like light, scaling and focus were identified as factors that could affect the image analysis of the recorded experiments.

The focus areas regarding the light conditions were to secure a good contrast between the powder afloat on the bath and the bath itself, and to minimize the glare which could compromise the results. Other than trying different lightning in the room, a cloth of black textile was placed on one of the sidewalls and under the model, in addition to covering a nearby wall to prevent glare.

A fixed mount for the camera was built on the top of the model. This ensured an equal distance between the camera and the bath surface, which provided a fixed scale. Different settings on the camera were adjusted, particularly the focus and brightness. Apart from improving camera conditions for increased reproducibility, a fixed feeder mount was built. This assured an equal placement of the feeder mechanism through all experiments. Four feet, each attached at a corner of the model, were installed to provide a better weight distribution for the model, thus further securing a horizontal bath in the leveled model.

In an attempt to make the water model behave more like an industrial cell, the bubbles generated from the anode tubes simulating carbon dioxide gas, were to be enhanced. A curved plate, with the shape of reversed gutter or a hood, was installed above each anode tube, thus making it possible to collect and convert the many small bubbles into fewer and larger bubbles. The installed tubes were angled toward the anode gap. A simplified sketch of this enhancement can be seen in Figure 4.14. Splashing of bath could also be observed after this installment, see Figure 4.13, a phenomenon observed in the industry [26].

Results

The water model after optimization is shown in Figure 4.13. Fixed mounts were given both the camera and feeder, and curved plates were installed above the anodes. Feet were installed at at every four corners of the model.
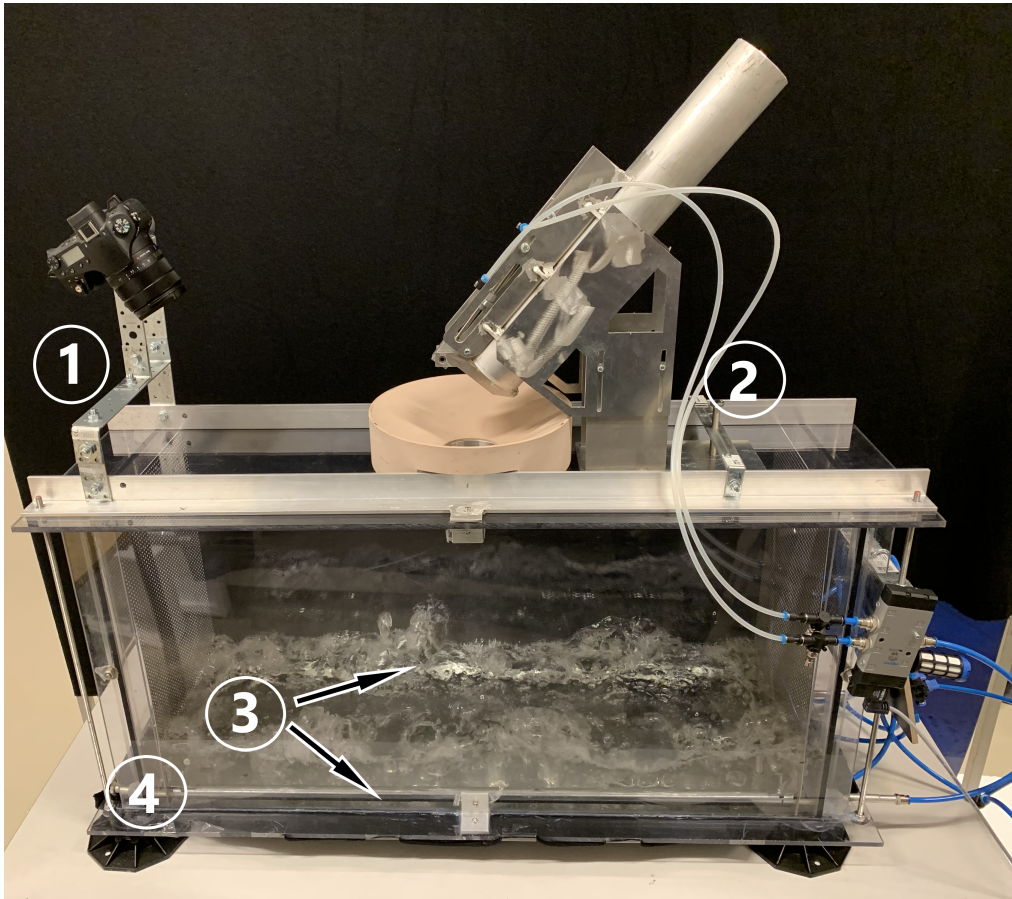
Figure 4.13: Water model used for the experiments after optimization. 1) Fixed mount for the camera 2) Fixed feeder mount 3) Curved plates above the anode tubes for improved bubble evolution 4) Foot.

Figure 4.14 shows a simplified sketch of the effect of the installed curved plates above the anode tubes. Many small bubbles were collected and formed into fewer and larger bubbles. The curved plate was installed with an incline to lead the release of the enhanced bubbles into the anode gap.
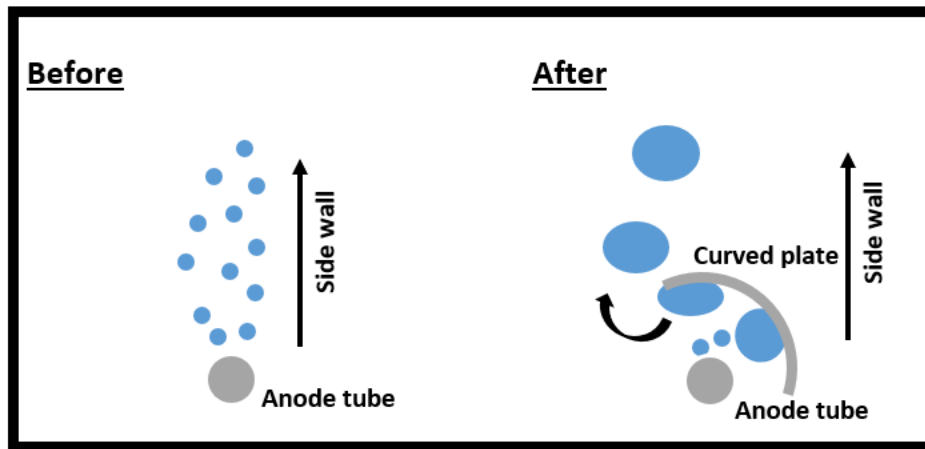
Figure 4.14: A simplified sketch of the the enhanced bubble formation after the installation of curved plates above the anode tubes, as seen from the end of the model.

4.7   Intitial experiments: Discussion

Observations and recordings done in the industrial cell at Alcoa Mosjøen provided better understanding of the aluminium production process. It also provided some guidelines on how to optimize the water model and determine the powder to be used as alumina to increase similarity to industrial cells. Recordings were processed in ImageJ and MATLAB for comparison to the results produced in water model experiments, later presented and discussed in this thesis.

Among the different powders tested, Natreen sprinkle sugar proved to be the most suitable powder for water model studies. Since Natreen is an artificial sweetener mainly consisting of maltodextrine and aspartame, pure maltodextrine was tried out as well in the water model. Maltodextrine caused handling difficulties as it got stuck in the feeder, providing discontinuous dispersion of powder into the bath. Another artificial sweetener by the brand Sukrin was tried out, but dissolved too quickly when bubble produced movement was included.

Crushed and frozen Natreen dispersed into water near freezing point is comparable to alumina dispersion and dissolution in an industrial cell. Despite different shape and size of crushed Natreen and alumina, they are analogous in terms of raft formation on a liquid surface under certain conditions. Water freezes around chunks of Natreen powder to form rafts in the same way cryolite freezes around alumina particles, as explained in Section 2.4.

A benefit of Natreen is that it fully dissolves in water without significant discolouration, or causing other disturbances on the surface when observing raft formations. Nevertheless, a high content of fines tends to increase dust production that attaches to nearby surfaces. This inconvenience may disturb recordings and image processing when conducting experiments in the water model.

PSD is calculated based on equivalent diameters of the crushed Natreen particles. This method does not give the exact distribution of powder, but provides a sufficient estimate. A disadvantage with this method of particle measurement is that each image has to be analyzed manually. Limitations set for the smallest particles to be obtained are determined by the operator capturing and analyzing the image, and can be varied until satisfying results are achieved. The settings of each image should be the same when performing this type of particle size analysis and can be done in ImageJ if the process

is scripted. However, this requires high quality SEM images with constant brightness and contrast settings for each image.

The fact that crushed and frozen Natreen, dispersed in cooled water, showed highest degree of correlation with alumina dissolution was a serendipitous discovery. The powder was randomly hand-crushed in the container upon small-scale testing. From a sample of the large-scale test, where a bigger sample of hand-crushed powder was used, the PSD was determined and further used as reference for the fine and coarse batches used in water model experiments. The hand-crushed testing batch was the only reference used to determine PSD of powder to be used in experiments. Due to Covid-19 laboratory access was restricted, and controlling the PSD in the first batch was difficult as this was performed at home. This resulted in a high fines content, perhaps too high for experimental testing.

Figure 4.8 represents the cumulative distribution of particle size for the four different crushing procedures tested, as well as the hand-crushed and fine batch for reference. When producing the results of PSD for the fine and coarse batch, only particles smaller than 100 μm were included although larger particles were present. These simplifications were performed to display the main distribution of particles present. From the coarse and the fine batch, only 1.6% and 0.9% of the measured particles were larger than 100 μm, respectively, giving a small amount of particles referred to as "coarse" at aluminium smelters. Additionally, the fine and coarse batch contained 60% and 80% particles smaller than 20 μm, respectively, meaning that they both had a high level of what the industry referrers to as "superfines".

Crushing procedure P2 was selected from Figure 4.8 as it resembled the PSD in the hand-crushed batch which initially gave good results in the water model during powder determination. However, as seen in Table 4.3 and Table 4.4, the coarse batch resembles the PSD of crushing procedure P1. Controlling PSD during powder crushing proved to be a difficult task. Better crushing techniques such as using a ball mill or similar should be considered. More effective ways of measuring and determining PSD would also be beneficial, as the method used in these experiments was time consuming, whilst uncertainties were poorly constrained.

Improvements on the water model concerning increased reproducibility, more specifically the fixed camera and feeder mount, are shown in Figure 4.13. With the camera mount installment, the distance between the camera and the bath became constant, thus giving a fixed scale for every test. This made the goal of an automated analysis more achievable. The fixed feeder mount secured a more equal feeding and dispersion of powder in all the experiments.

The visit at Alcoa Mosjøen influenced the enhancing of the CO_2-simulating bubbles from the anode tubes. The original bubbles generated in the model were small and of high frequency. With the installment of a curved plate above both the anode tubes, the small gas bubbles were accumulated and emerged as bigger bubbles when released from the reversed gutter. A sufficiently high gas flow produced some of the same splashing effect as observed in industrial cells [26]. Splashing was also observed at Alcoa in Figure 4.1 and in the video linked in Section 4.1.

Several factors that affected a more automated image analysis, and made this objective harder to obtain, were identified during the initial post-processing. Especially different light conditions, both in the room of the experimental testing and on the model itself, made the analysis challenging. This is discussed in more detail in the post-processing discussion in Section 7.3 and 8.2.

5 Main experiments

Experiments were performed on the optimized water model as described in the preceding chapters. The main objective of the following experiments was to determine the relative importance of PSD, bath temperature and bubble induced convection on raft floating times. The relative importance was quantified by factorial design - as described in the the following section.

5.1 Factorial design

Factorial design is widely used in statistical analysis for parametric studies where multiple factors are investigated at the same time. It is typically used to describe the influence of the individual parameters, along with the interaction between them. The basis of a factorial design consists of m parameters, which is studied at n-levels. This will provide a set of n^m experiments to be conducted. Standardized factorial designs are often constructed with each parameter only being investigated at two levels, representing a low and high value [26, p.209] [33, Ch. 5-6]. This aims to increase the simplicity and practicality of the design.

This parametric study is constructed in a similar fashion. Three parameters are set with two levels (high/low) for each factor. To account for all parameters and levels, a total of $2^3 = 8$ experiments needs to be conducted. A randomized order is desirable to avoid external influences. However, in this study it is assumed that external factors are of little to no impact. Therefore, the experimental matrix shown in Table 5.1 was computed in MiniTab, a statistical software, with some customization to the randomized order. These adjustments were made to simplify the experimental execution and reduce chances of condensation from temperature variations. In order to obtain statistics, each experiment was repeated three times, resulting in a total of 24 experiments.

Table 5.1: Experimental matrix for water model experiments.

Experiment	PSD	Bubble frequency	Temperature water
1-3	Fine	Low	Low
4-6	Fine	Low	High
7-9	Fine	High	High
10-12	Fine	High	Low
13-15	Coarse	Low	High
16-18	Coarse	Low	Low
19-21	Coarse	High	Low
22-24	Coarse	High	High

5.2 Main experimental setup

All experiments conducted in the water model were recorded by a top mounted Sony Cybershot DSC-RX10 IV camera, aiming to document and determine the floating time of fed powder. Natreen powder was loaded into a container (1 L), simulating one dose of alumina.

Two different PSDs of the Natreen powder were used, as displayed in Table 5.2, representing alumina containing fine and coarse particles. The coarse batch was crushed after procedure P2, described in Section 4.5, listed in Table 5.2.

Table 5.2: Different crushing methods for each batch of powder.

Batch	Power	Time	Number of cycles
Fine	High	5 sec	5
Coarse	Low	3 sec	3

The experimental containers were placed in an ultra-freezer with an average temperature of -80°C. To ensure homogeneous temperature of the whole container they where stored in the freezer for at least 48 hours before experimental implementation. Water used in the model during experiments was cooled down with ice placed inside arranged compartments of the model as described in Section 4.6.1. Water was circulated by using the convection tubes to ensure even distribution of temperature. Temperature was measured by a VWR hand held thermometer (VWR catalog number: 620-0916). Temperature of the powder placed in the feeding cylinder was measured by a Fluke 54 II B thermometer, and listed for each experiment.

The airflow in the bubble producing tubes was measured by filling a 16 L tank with water, placed in a water filled container with a tube put into the 16 L tank, Figure 5.1 illustrates the setup. This tube was further connected to the water model airflow panel. When the airflow was turned on, a timer started, and then stopped when the airflow had pushed the 16 L of water out of the tank. This procedure was conducted three times each for the "high" and "low" levels on the water model, and an average airflow was calculated.
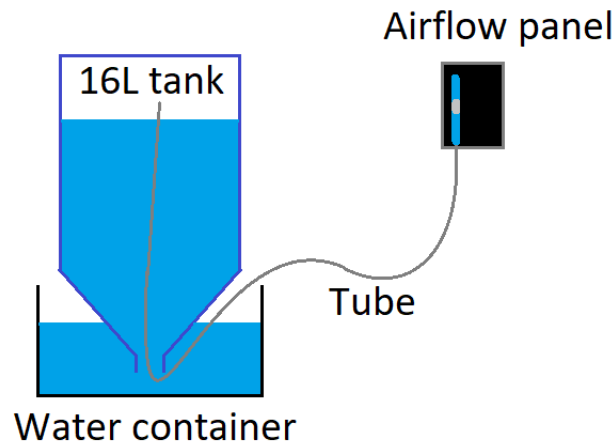
Figure 5.1: Illustration of the setup for airflow measurement.

5.3 Experimental implementation

Experiments were performed after the generated matrix listed in Table 5.1. When the model was assembled and filled with water and ice, the feeder placed on top of the model was filled with powder from the 1 L container. Powder was released into the bath when the camera was set to record, temperature of powder and bath were measured and correct bubble frequency was enabled. The experiment was considered finished when no more rafts were floating on the water surface. Water inside the model was changed every third experiment.

5.4 Post processing data

Following the experiments, the raw data (i.e. video) from each experiment was analysed using different tools, each described in this section.

5.4.1 MATLAB

MATLAB is a programming language developed by MathWorks. Cleve Moler, the computer science chairman from the University of New Mexico (UNM), started the development in the late 1970s, but it was not released until 1984. It is mostly used for numerical computing with applications such as plotting data, matrix manipulation, algorithm-implementation and more. In this thesis MATLAB was exclusively used for calculations with matrices and the plotting of simulation-data [34].

5.4.2 Processing the recordings

The processing consists of three main steps and was used for both industrial and modeled data:

1. Splitting the video into images with ffmpeg.

2. Adjusting the image-stack and extracting useful data in .csv files with ImageJ.

3. Producing graphs from the .csv files with MATLAB.

ImageJ cannot process .mp4 formats directly, requiring transformation of these recordings into processable images. This is done using a script with ffmpeg. The script moves the files into separate folders and ffmpeg splits the video into two .jpg images per second of video. Lastly, a manual removal of excessive images is required to avoid using images from before the initial feeding.

The splitted image stack from step one is then imported as an image sequence in ImageJ for further processing [31]. Firstly, the scale needs to be set to be able to estimate area and later compare area between experiments. This is done by importing a picture with a measuring tape beside the model (level with the bath surface), and using the "Set Scale" function in ImageJ. The image stack is then cropped around the bath, so that only the bath surface is visible. Adjustments are applied to the images, which includes changing image type to 32 bit and adjusting the brightness/contrast to enhance visual raft separation from bath. After these alterations are correctly executed, the threshold is manually set to best represent the change in surface area. This is done with rafts being marked with red and unchecking the box for "set background pixels to NaN"

when applying. To extract the useful data into a .csv file, a macro is needed to collect the following: area, area fraction, and stack position.

MATLAB is used to visually present the data as graphs with surface area plotted against time [35]. The .csv files from step two are read and processed as matrices. These are then used to calculate average values for the surface area seen from above, standard deviation, and a confidence interval based on Student's t-distribution. Every parameter variation is plotted with average values and a 95% confidence interval for the three experiments. A function called "Filled area plot" is used to shade the confidence interval [36]. Lastly, three data points (start, halfway, end) were used to calculate dissolution rates of different areas of each graph as illustrated in Appendix B.

6   Results

A total of 24 experiments were performed in the following order displayed in Table 6.1. The floating time was assessed manually based upon videos from each experiment. The time evolution of the experiments is represented graphically and visually in figures 6.1-6.16. Each graph represents averages of three experiments with the same combination of parameters with the x-axis set as the average floating time for these conditions (as of Table 6.1). A 95% confidence interval is included in each figure. The y-axis shows the change in average surface area (cm^2) of the rafts from the initial feeding (first contact with bath) to full dissolution (no powder left on bath-surface). This is plotted against the dissolution time (s) of these rafts on the x-axis. The surface area displayed on the y-axis is not reduced to zero after full dissolution, as disturbances in the images have a continuous presence. The impact of these disturbances (bubbles and glare) varies between experiments. It appears visually at the end of the graph when the powder is fully dissolved (no raft area), and only the area affected by disturbances is left. For example, full dissolution is achieved in Figure 6.1 and 500 cm^2 in visual disturbances are still present at the end of the graph when no powder is left on the surface.

Table 6.1: Measured values of each parameter listed in order of the matrix in Table 5.1, in addition to powder temperature and floating time.

Experiment	D_{50}	Bubble frequency	T_{water}	T_{powder}	Time
[#]	[μm]	[L/min]	[°C]	[°C]	[s]
1	10	75	1.0	-54.5	500
2	10	75	1.0	-65.0	540
3	10	75	1.2	-56.1	550
4	10	75	7.9	-48.0	260
5	10	75	7.0	-58.9	330
6	10	75	7.2	-48.4	320
7	10	200	7.0	-65.1	185
8	10	200	7.4	-60.1	180
9	10	200	7.9	-49.7	210
10	10	200	1.2	-36.1	260
11	10	200	0.9	-47.7	275
12	10	200	1.4	-41.8	240
13	15.5	75	7.1	-54.0	60
14	15.5	75	7.7	-46.0	65
15	15.5	75	7.6	-56.1	70
16	15.5	75	1.3	-69.8	135
17	15.5	75	1.0	-57.3	120
18	15.5	75	1.3	-51.2	115
19	15.5	200	1.0	-47.1	45
20	15.5	200	0.7	-40.1	50
21	15.5	200	0.7	-33.1	55
22	15.5	200	7.1	-45.2	35
23	15.5	200	7.1	-54.8	37
24	15.5	200	7.1	-45.6	40

Figure 6.1: Average surface seen from above in cm^2 plotted against time (s) for experiment 1-3 (fine PSD, low bubble frequency, low water temperature).

Figure 6.2: Sample images of raft formation and dissolution after feeding of Natreen in experiment 1, video available at (`https://youtu.be/q02Au7U1nSE`).

Figure 6.3: Average surface seen from above in cm^2 plotted against time (s) for experiment 4-6 (fine PSD, low bubble frequency, high water temperature).

Figure 6.4: Sample images of raft formation and dissolution after feeding of Natreen in experiment 4, video available at (`https://youtu.be/gFDAfhY_YzM`).
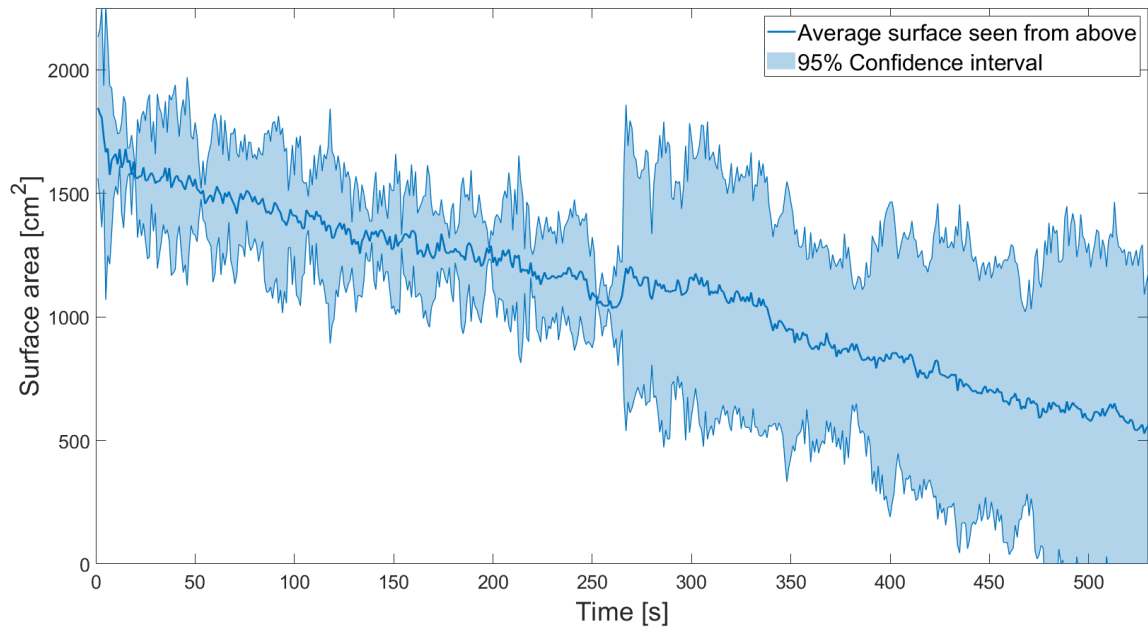
Figure 6.5: Average surface seen from above in cm^2 plotted against time (s) for experiment 7-9 (fine PSD, high bubble frequency, high water temperature).

Figure 6.6: Sample images of raft formation and dissolution after feeding of Natreen in experiment 7, video available at (`https://youtu.be/oa8utBlcrvE`).
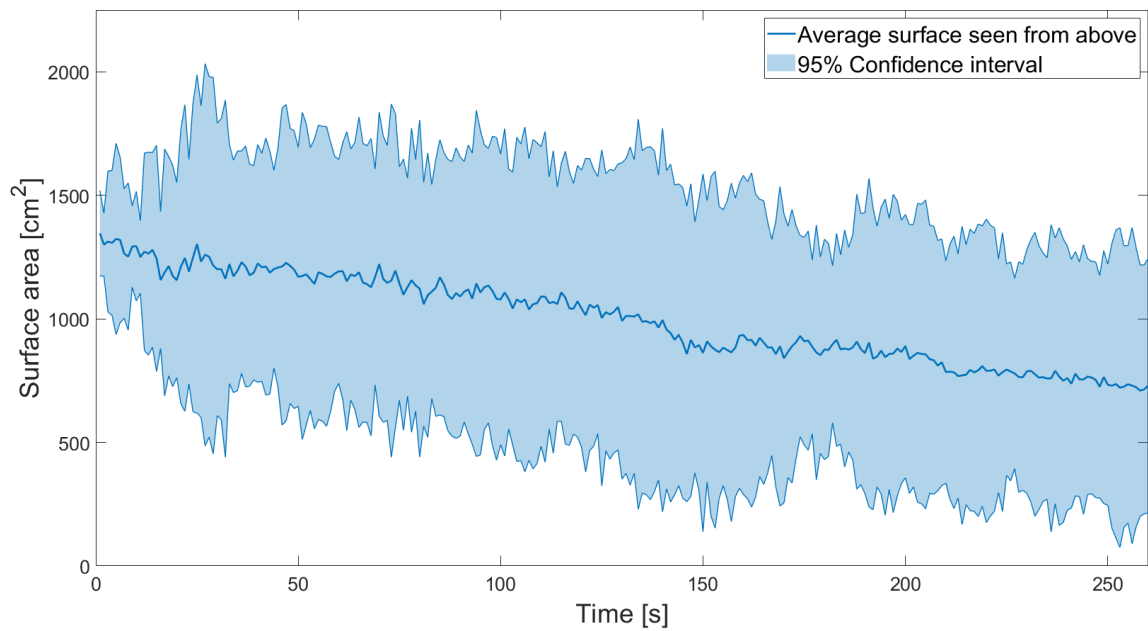
Figure 6.7: Average surface seen from above in cm^2 plotted against time (s) for experiment 10-12 (fine PSD, high bubble frequency, low water temperature).
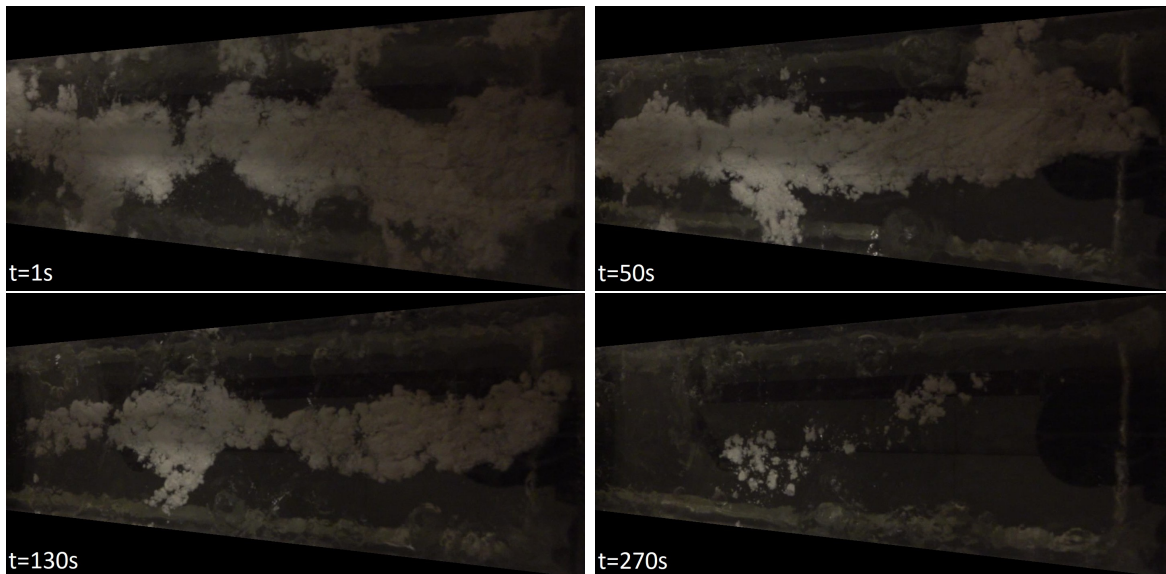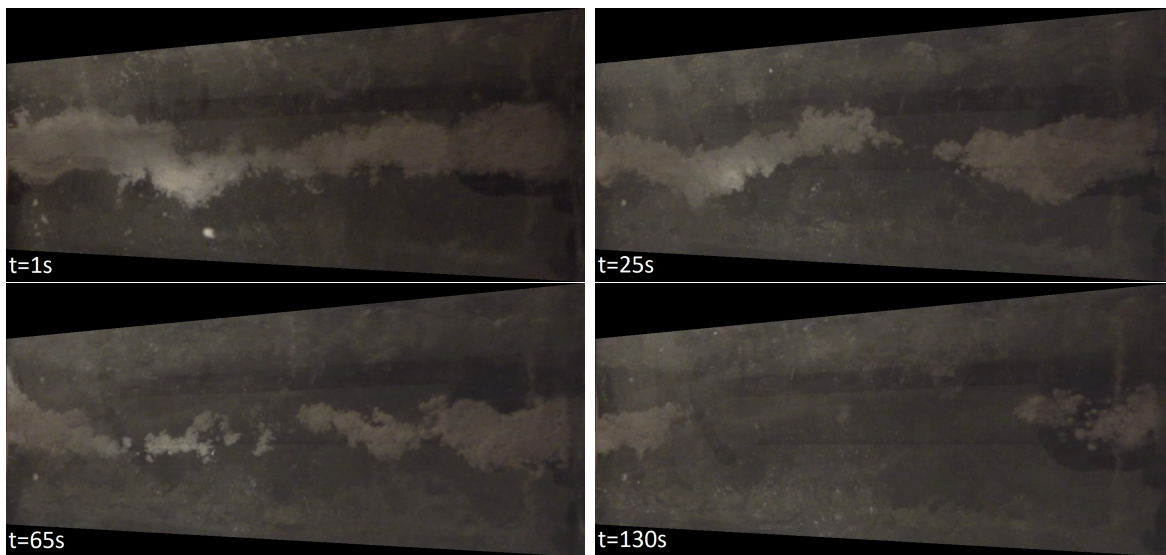

Figure 6.8: Sample images of raft formation and dissolution after feeding of Natreen in experiment 12, video available at (`https://youtu.be/5DKAXvKYkHs`).
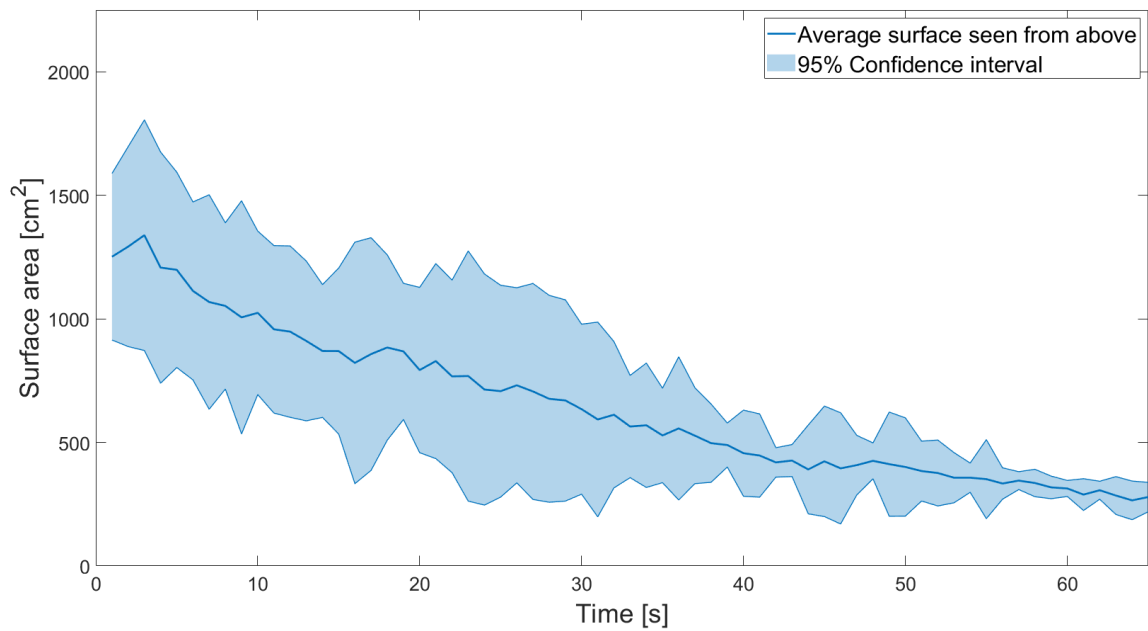
Figure 6.9: Average surface seen from above in cm^2 plotted against time (s) for experiment 13-15 (coarse PSD, low bubble frequency, high water temperature).
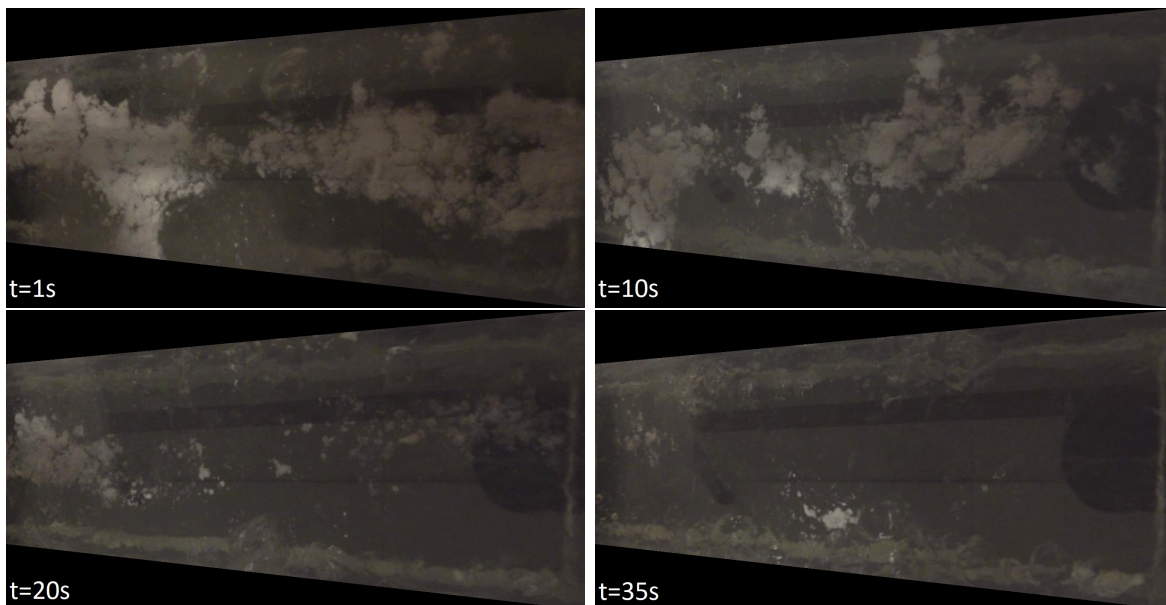
Figure 6.10: Sample images of raft formation and dissolution after feeding of Natreen in experiment 14, video available at (`https://youtu.be/5YyEhYcI12c`).
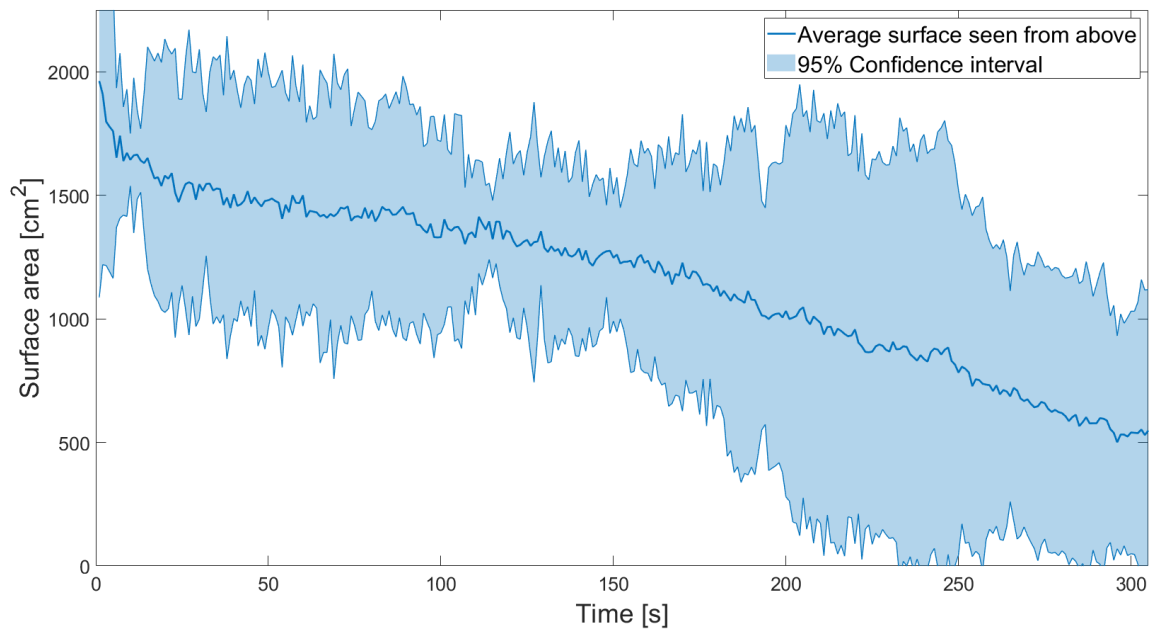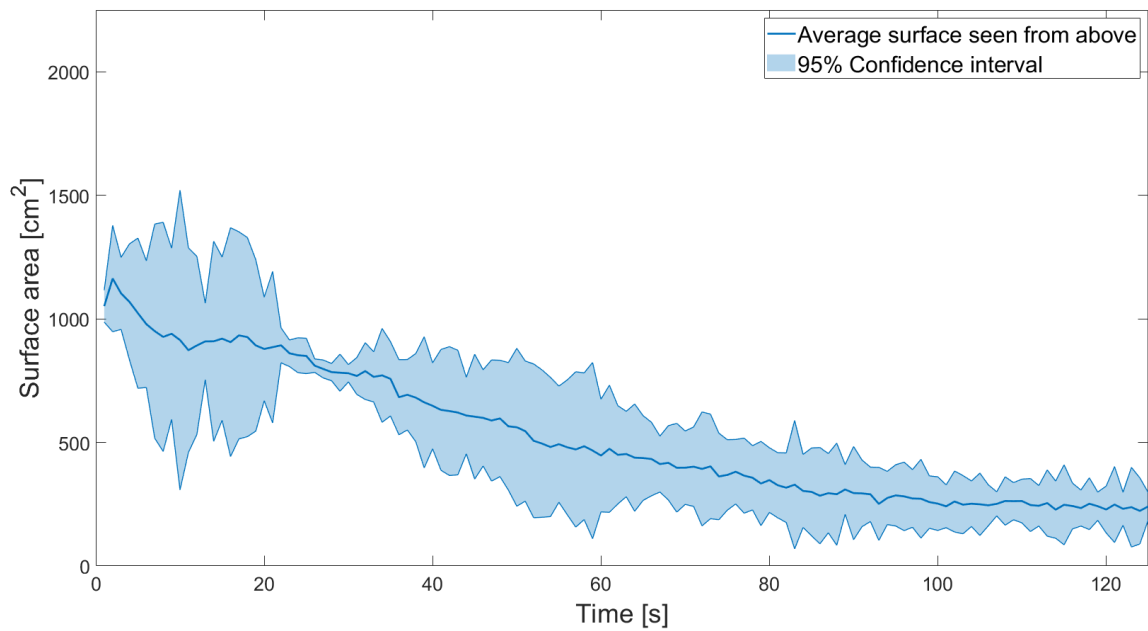
Figure 6.11: Average surface seen from above in cm^2 plotted against time (s) for experiment 16-18 (coarse PSD, low bubble frequency, low water temperature).
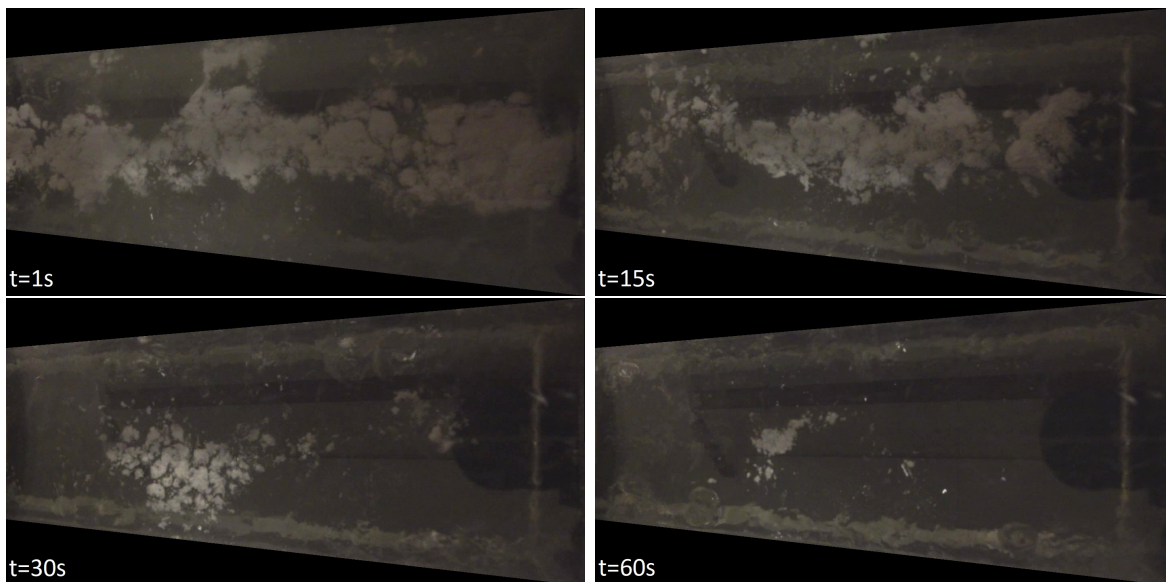
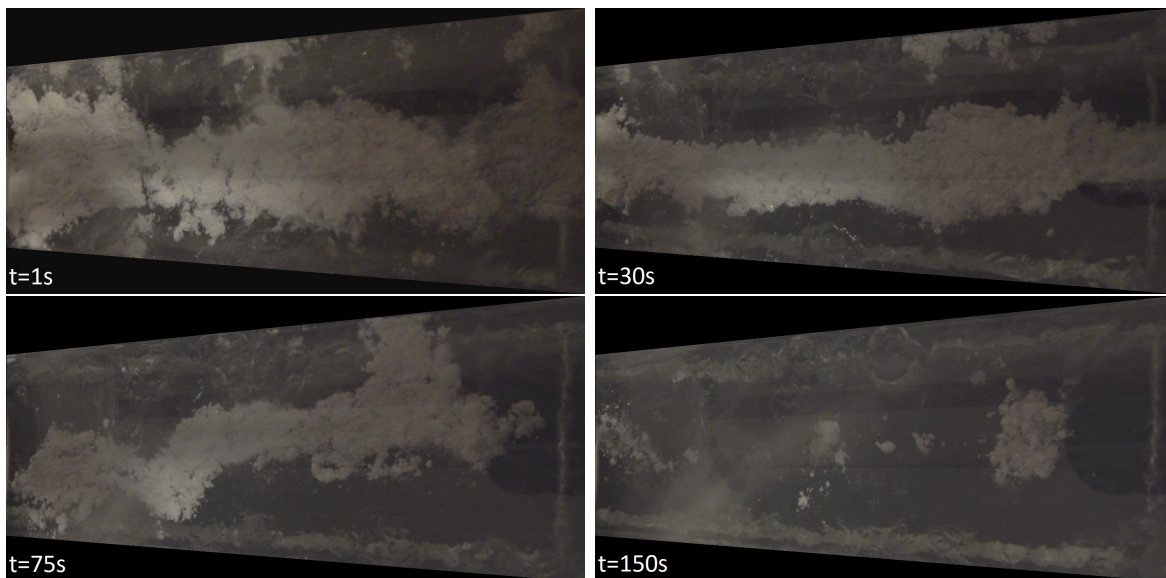**Figure 6.12:** Sample images of raft formation and dissolution after feeding of Natreen in experiment 17, video available at (`https://youtu.be/NLHiMuRDdWc`).
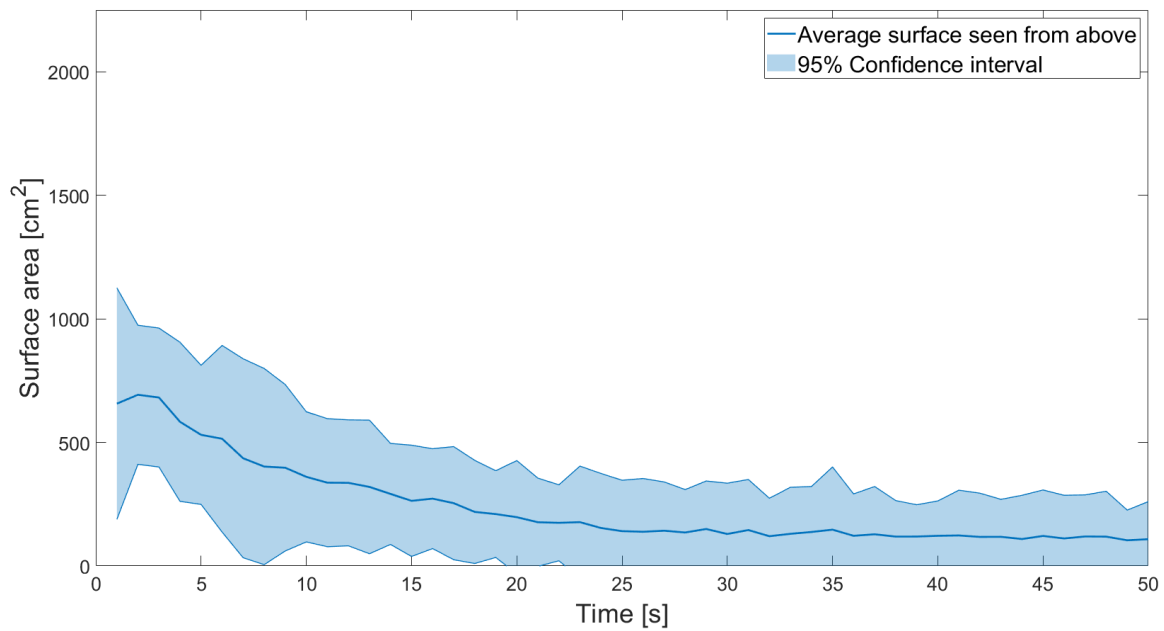
Figure 6.13: Average surface seen from above in cm^2 plotted against time (s) for experiment 19-21 (coarse PSD, high bubble frequency, low water temperature).
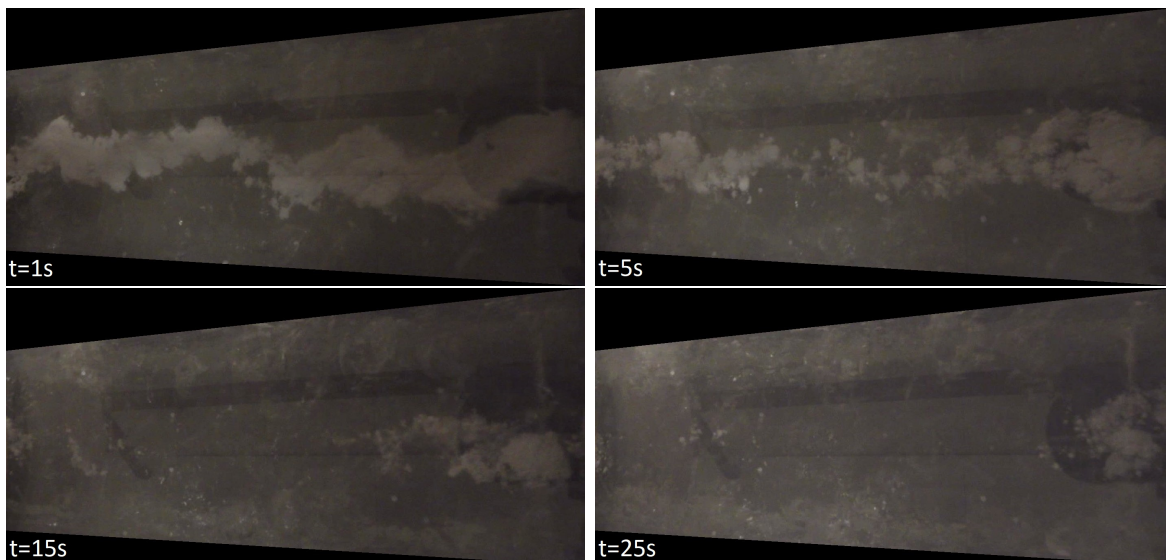
Figure 6.14: Sample images of raft formation and dissolution after feeding of Natreen in experiment 21, video available at (`https://youtu.be/rAYlcUwO8Xc`).
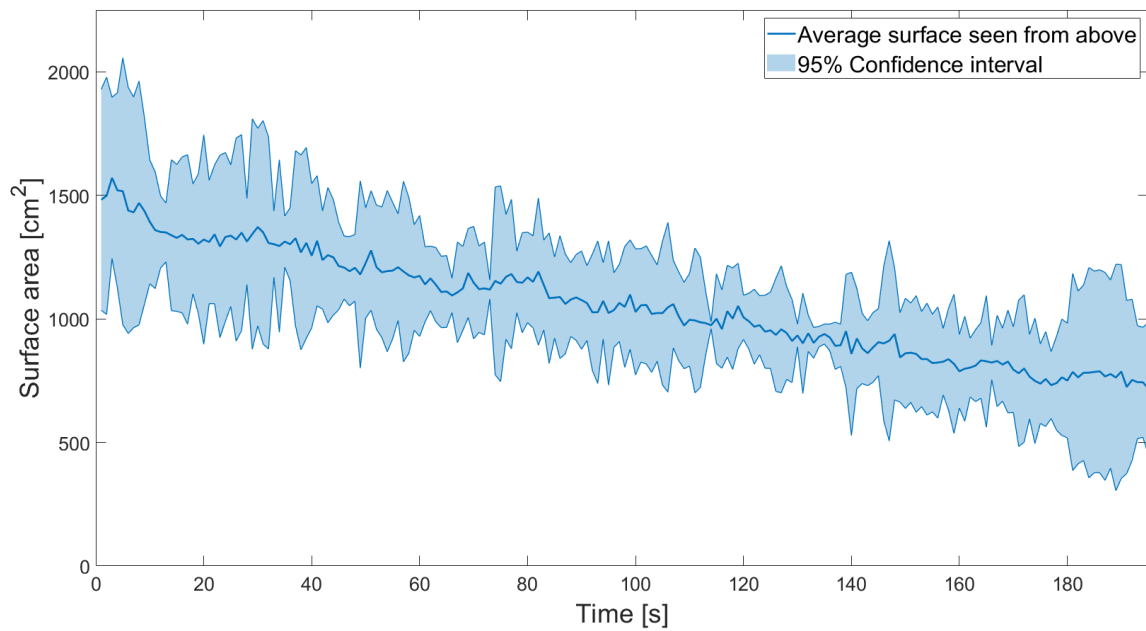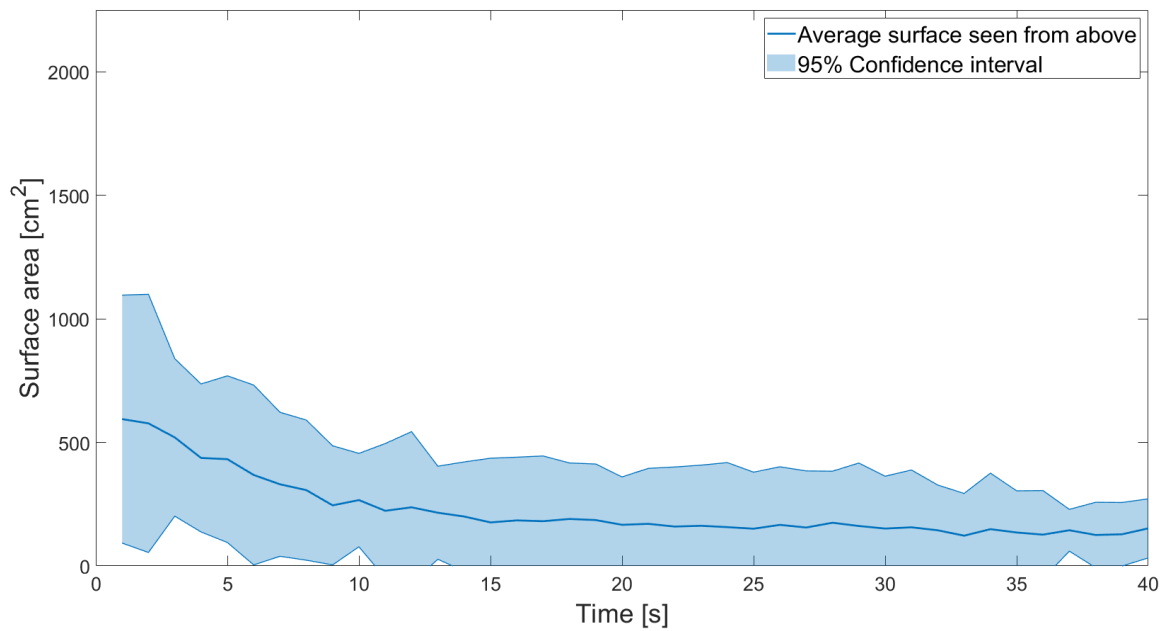
Figure 6.15: Average surface seen from above in cm^2 plotted against time (s) for experiment 22-24 (coarse PSD, high bubble frequency, high water temperature).
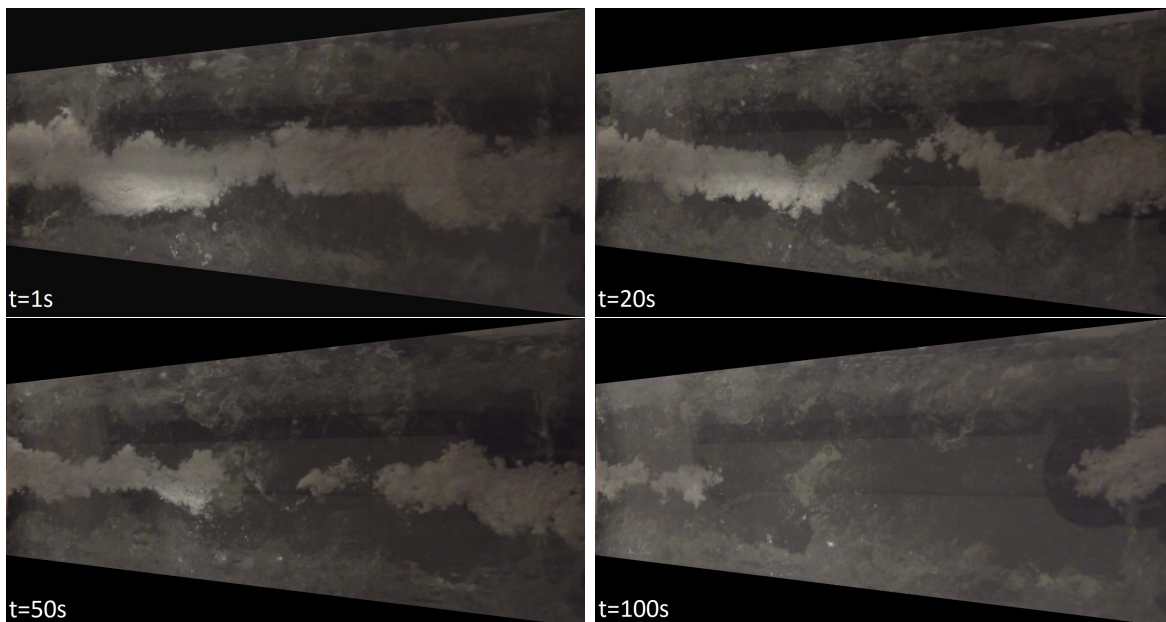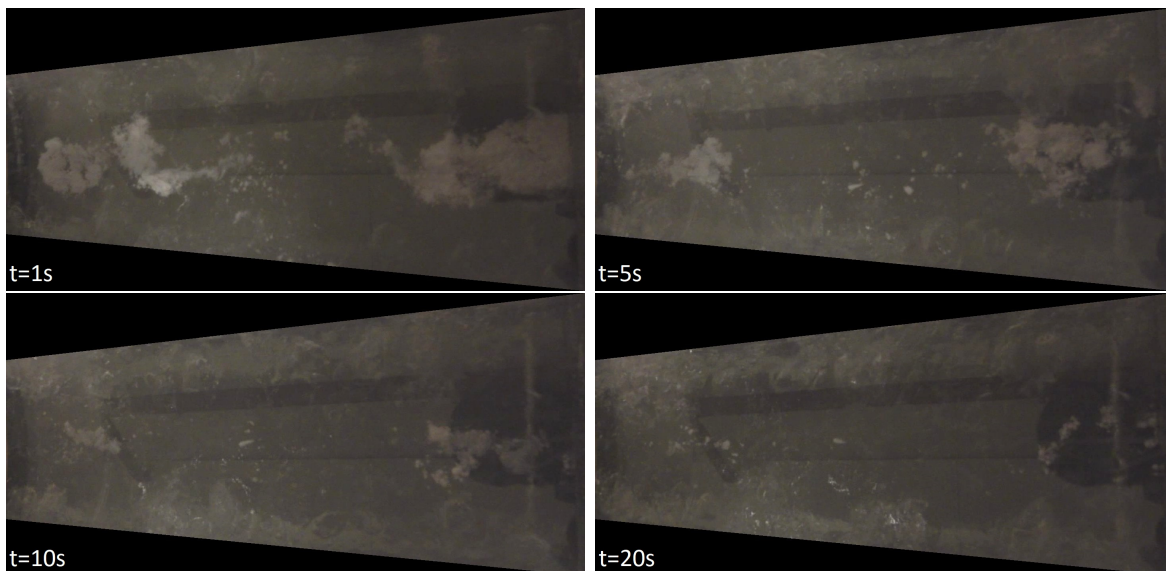

Figure 6.16: Sample images of raft formation and dissolution after feeding of Natreen in experiment 22, video available at (`https://youtu.be/Y78bkbD18X8`).

Industrial data from the visit at Alcoa Mosjøen is shown in Figure 6.17 and analyzed using the same procedure as the water model data. Corresponding to water model experiments, the graph sees reduction in surface area seen from above. As seen in Figure 4.1, some agglomerates and disturbances are present in the images after the initial dissolution of alumina. This contributes to the graph not dropping to zero in surface area, rather continuing in a sideways pattern. Based on this knowledge, the graph visually indicates that the dissolution for this particular case takes approximately 25 seconds.
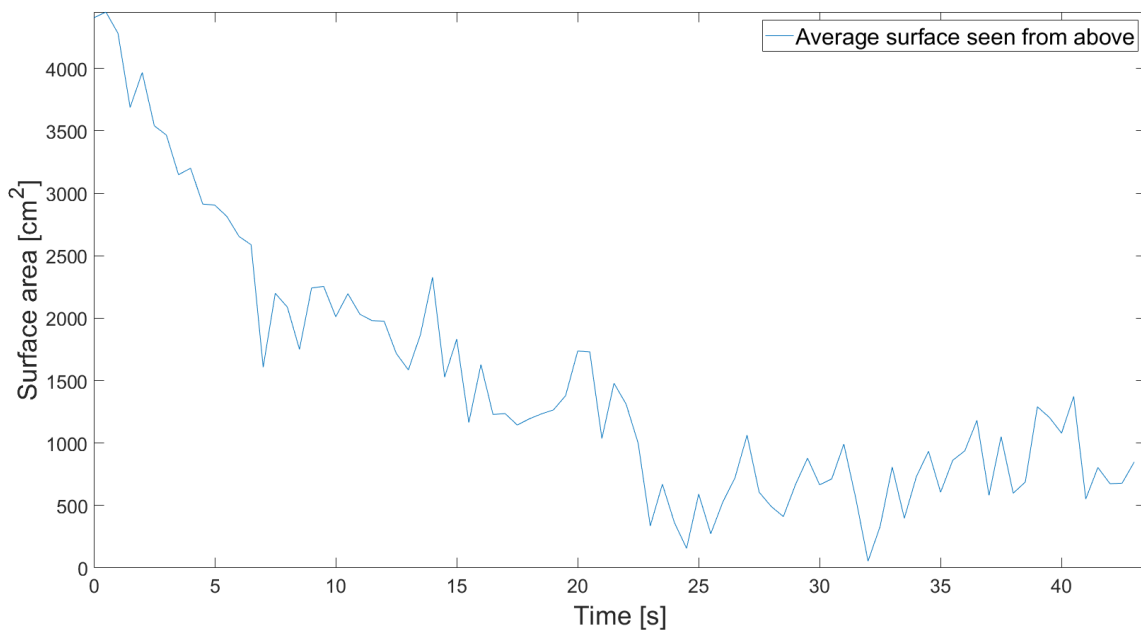
Figure 6.17: Average surface seen from above in cm^2 plotted against time (s) for a feeding in an industrial cell at Alcoa Mosjøen. The graph is generated by analyzing the recordings seen in Figure 4.1, video available at (`https://youtu.be/KooL0mzL5V0`).

The graphs presented in this chapter were used to calculate dissolution rates of the experiments. Three rates were calculated for each graph: initial (first half), final (second half), and total. The calculations used the slope of the lines to represent the dissolution rate. This is further explained and illustrated in Appendix B. The dissolution rates are displayed in Table 6.2 as both cm^2/s and $\%/s$.

Table 6.2: Calculated dissolution rates of the experiments.

Experiment	Total rate		Initial rate		Final rate	
[#]	[cm^2/s]	[$\%/s$]	[cm^2/s]	[$\%/s$]	[cm^2/s]	[$\%/s$]
1-3	-2.44	-0.13	-2.88	-0.16	-1.99	-0.11
4-6	-4.65	-0.24	-4.89	-0.25	-4.42	-0.23
7-9	-3.94	-0.27	-4.35	-0.29	-3.53	-0.24
10-12	-2.38	-0.18	-2.75	-0.20	-2.01	-0.15
13-15	-15.20	-1.21	-20.63	-1.65	-10.09	-0.81
16-18	-6.53	-0.62	-9.86	-0.94	-3.31	-0.31
19-21	-11.19	-1.70	-21.50	-3.27	-1.30	-0.20
22-24	-11.34	-1.91	-22.52	-3.79	-0.72	-0.12
Alcoa	N/A	N/A	-173.43	-2.34	N/A	N/A

The initial mean surface area of the fed powder after 1 s (x=1) is presented in Table 6.3. This illustrates the immediate dispersion and give an insight in the raft sizes formed right after feeding. Experiments 19-24 stands out with its low initial area.

Table 6.3: Initial mean surface area (cm^2) of fed powder in the form of rafts after 1 second.

Experiment	PSD	Bubble frequency	T_{water}	Initial mean surface area
[#]	-	-	-	[cm^2]
1-3	Fine	Low	Low	1846
4-6	Fine	Low	High	1963
7-9	Fine	High	High	1482
10-12	Fine	High	Low	1346
13-15	Coarse	Low	High	1251
16-18	Coarse	Low	Low	1051
19-21	Coarse	High	Low	657
22-24	Coarse	High	High	594

The charts shown in Figure 6.18 and Figure 6.19 were generated from the statistical software Minitab, and shows a regression analysis based on the results from the water model experiments which was run with a 2^3-factorial design. As described in Section 5.1, the parameters were tested in the water model with two different values for each parameter, see Table 5.1, and the effect of these two values is shown in Figure 6.18. Figure 6.19 illustrates the impact and significance for each of the parameters and parameter interactions tested in model.

Figure 6.18 addresses the impact of the variation of parameter-values tested. PSD, bubble frequency (gas flow rate), and bath temperature were tested at two levels, illustrated in the chart as "-1" and "1". A low bath temperature and bubble frequency, and a fine PSD are depicted as "-1", while "1" represents a high bath temperature and bubble frequency, and a coarse PSD. The effect of the two different parameter-levels is plotted against the mean of time in seconds, representing the mean floating time for the powder in the experiments. A low mean of (floating) time reflect a preferable fast dissolution.
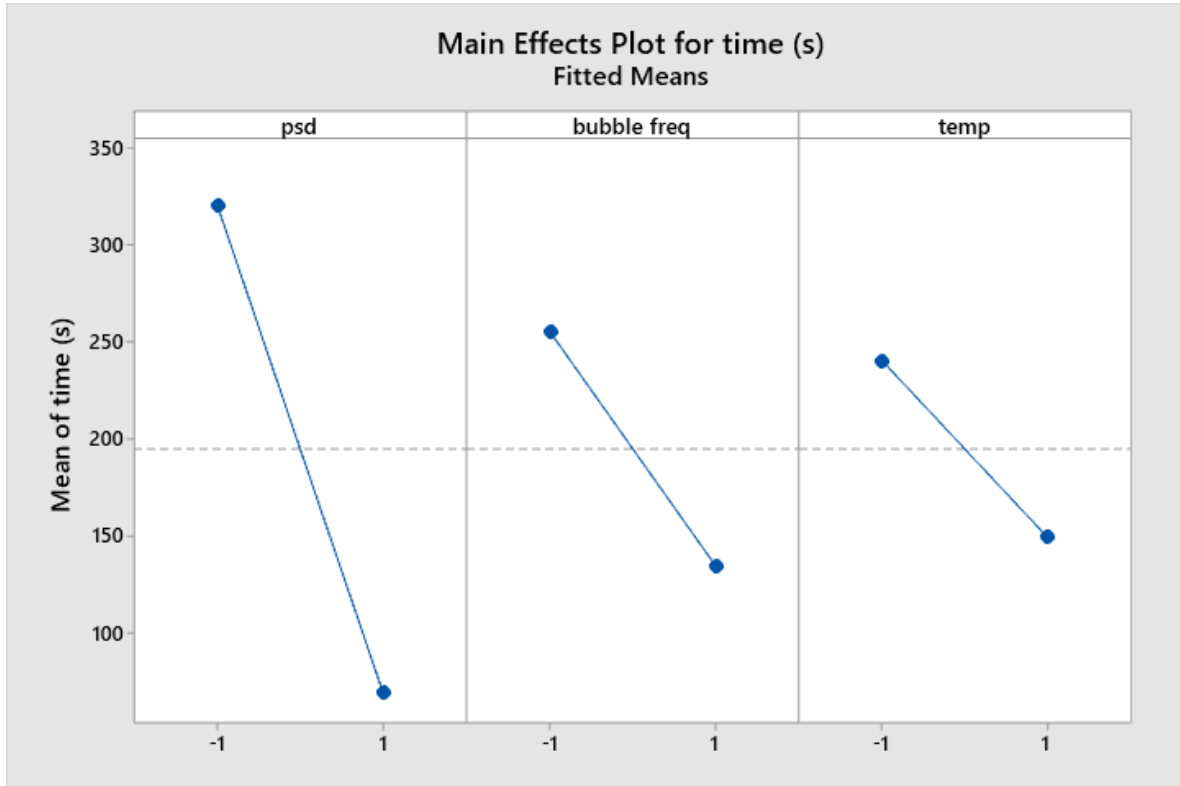
Figure 6.18: Main effect of the different parameter levels upon mean (floating) time (s). PSD, bubble frequency (gas flow) and bath temperature were adjusted between two levels in the experiments, here seen as "-1" (low/fine) and "1" (high/coarse) along the x-axis.

The chart in Figure 6.18 shows that a coarse PSD and a high bubble frequency (gas rate) and bath temperature gives a lower floating time. The level-change of PSD from fine to coarse, stands out as the parameter-change with the biggest effect on the floating time.

Figure 6.19 presents the standardized effect of the parameters and the interactions between them. Standardized effect describes the effect size as a quantitative measure and ignores the units of the different parameters. In this way, the effect of each parameter and parameter combination is presented with a dimensionless size. The red mark at 2.12 shows the limit of statistical significance. All the effects are above this value.
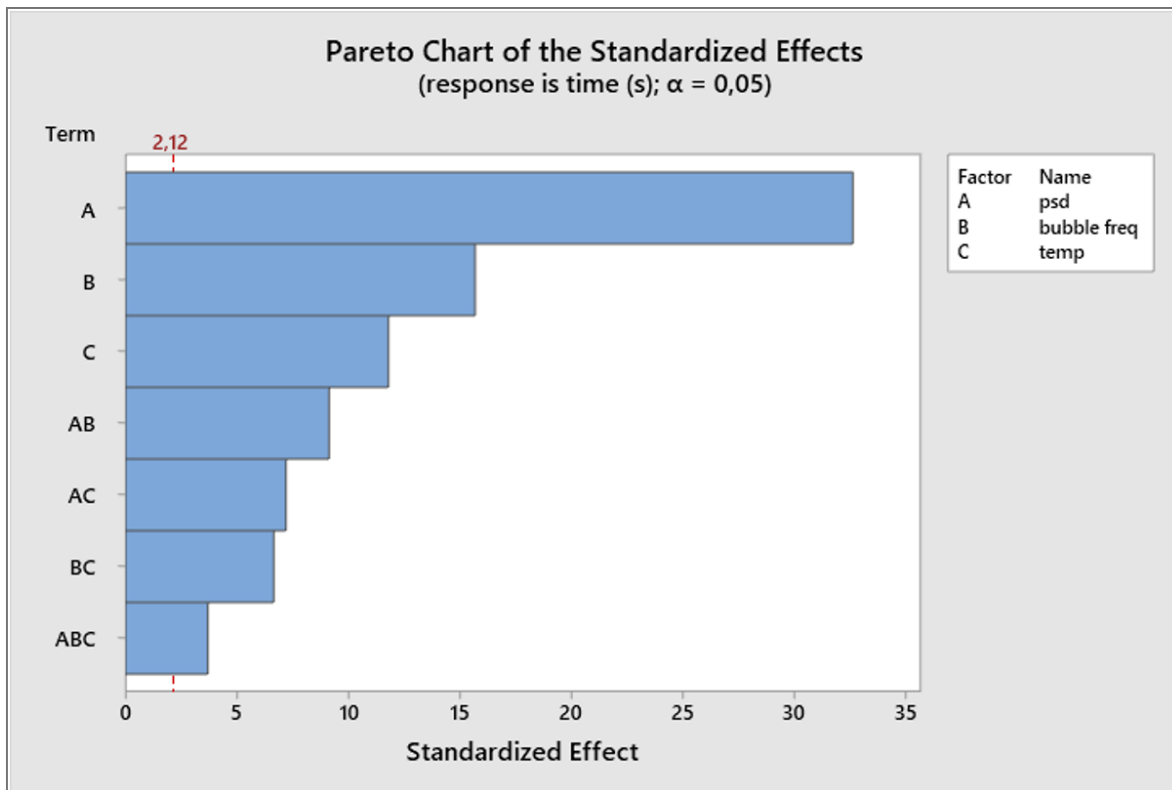
Figure 6.19: Pareto chart illustrating the standardized effects of PSD, bubble frequency, temperature and the interactions between them.

PSD has a considerable effect on the experiments compared to bubble frequency (gas flow) and bath temperature. As shown in Figure 6.19, PSD has around twice the effect as the the two other parameters

7 Discussion

7.1 Experimental method

The experimental work contained multiple sources of errors and variations. The powder fed was stored in an ultra-freezer for at least 48 hours to reduce the chance of temperature variation between tests. Nevertheless, the measured temperature still varied a significant amount throughout the experiments. This may have been caused by irregularities in the measuring itself, as it proved to be quite difficult to accurately measure the temperature of the powder in the feeder. Another thermometer could have been tested to improve measuring accuracy. Additionally, routines for more frequent washing of the metal rods used for measuring could be implemented since powder agglutinated on the rods. The water temperature was varying with less than one degree, likely influenced by ambient temperatures.

The visibility of powder in the recordings may be a source of deviation. Some powder continuously escaped the field of view of the camera, which in turn affected the measured surface area. This was mainly observed in experiment 7-12 and 19-24 when experiments with high bubble frequency were conducted. It can be seen in Figure 6.6, 6.8, 6.14 and 6.16 that powder becomes undetectable at the end of the images. A small blind spot was present in the model at the opposite side wall of the camera, but was identical in all experiments due to the fixed mount (see Appendix C). This spot was reduced by camera placement, but changes of the feeder hole position is required to allow visual contact with the entire bath surface.

External factors, like a change in room temperature or humidity, may somewhat vary between experiments. However, as the experiments were performed in a modern laboratory with automated systems controlling temperature and humidity (i.e. air-condition), external factors were deemed to have insignificant impact. These assumptions made way for a customised and more convenient test matrix, based on factorial design. The possible effect from increased saturation of dissolved Natreen in the bath during the experiments was neglected, as the highest achieved saturation was approximately 1.5% of the solubility limit (calculated in Appendix D).

7.2 Results from experiments

PSD had a more influential effect on the floating time than the bubble frequency (gas flow) and bath temperature. Figure 6.19 shows that PSD had almost double the effect relative to the two other parameters. The high fines content resulted in a much longer dissolution time for the fine batch compared to what was observed with the initial hand-crushed batches. In the coarse batch, the presence of larger particles contributed to a significant decrease in dissolution time, with the effect being strongest in experiments 19-24. This may be attributed to the blender malfunction during powder crushing for these experiments, making it difficult to ensure an equal PSD in all samples. This should be considered as a potential source of error, since PSD were not measured for these samples individually. Both batches could be screened to secure a lower content of fines, but the high fines content was assumed to cause Natreen to stay afloat and form the desired rafts investigated in this study.

The graphs presented in Chapter 6 show considerable differences in dissolution between experiments. These are quantified as the dissolution rates calculated in Table 6.2. In experiment 1-12, the results with fine PSD show a gradual decrease in surface area over a span of 200-540 seconds. These graphs have a gentle slope, which represents an even dissolution spread out across the whole length, observed in all the dissolution rates. In experiments 13-24, the coarse PSD shows a faster decrease in area, spanning across shorter time intervals from 40-120 seconds. The corresponding graphs have much steeper initial slopes, confirmed by the initial dissolution rates being significantly higher than the final and total rates. Dissolution rates in Table 6.2 are on average much faster for experiments with a coarse PSD versus the fine PSD. Both initial and total dissolution are faster for the coarse PSD, with graphs having an increased gradient and shorter time-spans. This coincides with literature and previous research, which shows high fines-content having a negative impact on dissolution, especially the fraction below 20 μm [6]. Additionally, Gylver et al. [20] found an alumina dissolution rate of 0.8 g/min (-0.33 %/s), which is closely related to multiple dissolution rates found in this study. In particular, the total rates of experiment 4-9 and multiple of the final rates shown in Table 6.2.

Bubble frequency is the second most influential parameter, as seen from Figure 6.18. Studies have found that increased bath surface and circulation appear to have a strong influence on floating time in industrial cells [22]. The correlation between the gas flow rate, in this study presented as bubble frequency, and current density can be

calculated using Faraday's law, thus enabling to simulate changes in the current density by varying the gas flow rate [23] [28]. Calculations made in Appendix A links the gas flow rate from experiments to anode current density using this correlation. It is noted that the measurement of bubble frequency was significantly simplified, only providing an approximation to industrial values. However, the calculations results in current densities of 0.7 and 1.8 A/cm^2 for the gas flows of 75 and 200 L/min, which is similar to industrial values of 0.8-0.9 A/cm^2 [1, p.42]. As seen from the plot in Figure 6.18, high bubble frequency gave a reduction in floating time.

Variations in water temperature had the least influence on dissolution time, as seen in Figure 6.18. Lavoie et al. [6] points out the importance of superheat, as initial dissolution is heat-transfer limited. Yang et al. [14] found that decreased superheat reduce initial dissolution rate but increase secondary dissolution time in laboratory studies. Gylver et al. [22] could not conclude with any influence by the superheat when studying the behavior of rafts in industrial cells.

Experiments 19-24, shown in Figure 6.13 and 6.15, stands out with a considerable lower initial mean surface area of the powder, presented in Table 6.3. These experiments were run with a coarse PSD and a high bubble frequency. Compared to the experiments run with a fine PSD and a high bubble frequency (7-12), the same trend is shown, although not as significant. Figure 6.4 (low bubble frequency) shows powder initially dispersed nearly in the full width of the bath surface. Compared to the experiment shown in Figure 6.6 (high bubble frequency), powder is dispersed only as a thin raft in the middle of the bath. Overall, these observations may indicate the positive effect of increased gas flow (bubble frequency) upon dispersion and initial dissolution of the powder, also presented by Chesonis and LaCamera [23].

During experiments some interesting powder behaviors were observed. Especially during the experiments with fine PSD, where a small agglomerate occasionally attached to the rigid cathode (bottom plexiglas) when fed (shown in Appendix E). These agglomerates contained dry, undissolved powder and small pockets of air, in addition to a combination of frozen bath and powder. Similar structures were found in industrial rafts analysed by Gylver et al. [21]. Some separated rafts tended to gather at the ends of the model close to the ice chambers, both for the fine and coarse batch, particularly when a high bubble frequency was introduced. This powder behavior caused some minor irregularities as a result of the blind-spont mentioned in Section 7.1.

The graph in Figure 6.1 spikes halfway due to a sudden divergence in the second experiment, displayed in Appendix F. A rapid increase in area appears in the individual graph of this experiment. The increase is caused by the threshold setting in ImageJ being affected by a small amount of condensation on the upper plexiglas. The condensation and rafts were in line prior to the spike, but the rafts drifted sideways, including both the rafts and the condensation as surface area. Multiple analyses of the recordings were carried out in an attempt to reduce the severity of the spike, only being partially successful.

7.3   Post-processing

A fully automated image analysis that could be run with a computer script proved to be more difficult than initially imagined. However, several measures were taken to increase reproducibility. Especially the light conditions appeared to be important as well as challenging in the attempt to meet this objective. As mentioned in Section 4.7, when analysing the videos, glare from both the curved plates above the anode tubes and the bubbles generated made it hard to set an even contrast threshold between the floating powder and the bath.

Colour contrast in images depends on both powder dispersion and light conditions. More powder dispersed on the bath surface contributes to more light reflected. Increased brightness correlates with increased reflections from both the top of the tank (plexiglas) and the bath surface. Reflections and glare both contribute to a more difficult analysis. This is a result of it interfering with the rafts in post processing, thus causing disturbances in the measured surface area. Actions were taken to avoid this as much as possible, but it proved to be challenging to completely eliminate.

7.4   Similarities to industrial cells

A graphical representation of an industrial feeding is shown in Figure 6.17. The result is limited to a single graph due to only one recording holding sufficient quality. The other recordings were out of focus, although with similar dissolution times, but discarded because of processing-difficulties. The figure share some similarities to Figure 6.13 and 6.15 both in steepness of the slope and initial dissolution time. The dissolution rates are -3.27 %/s and -3.79 %/s for the water model experiments, versus -2.34 %/s for the industrial feeding. This is a relatively close connection, and indicate that the water model experiments may be able to sufficiently simulate industrial cells.

The effects of parameter variations in water model experiments have shown certain similarities with observations made in industrial cells, and other studies regarding alumina feeding and dissolution. Although the variations in PSD, superheat and bubble frequency have some resemblance to industrial cells, there are some applications that are challenging to implement on the water model. Transformations in crystallographic forms of the alumina particles and the complex chemical composition of the electrolyte are the two main factors. The organic powder used in the water model has no phase transitions when exposed to mechanical crushing or temperature differences such as alumina. These phases have proved to have an impact on the crust formations in industrial cells as well as the dissolution rate of alumina [6]. This is not taken into account when comparing the water model to industrial cells.

The water model itself is significantly simplified regarding bath chemistry. Baths used in industrial cells has a complex composition of additives in addition to an important concentration of alumina. Concentrations of alumina close to its solubility limit has an influence on the dissolution rate as it becomes mass-transfer limited [6]. Bath used in the water model only contains one single phase of liquid, while multiple phases with different densities could increase its resemblance to industrial cells.

Lavoie et al. [6] points out the importance of feeder hole condition. Because the feeder hole limits available bath area and superheat, the thermodynamics in feeder holes are significant. The water model operates at room temperature, with a continuous bath area available. In the water model the feeder and feeder hole are designed and placed within industry standards, as mentioned in Section 4.6. During these experiments, the feeder hole remained open the whole time, and rafts were completely dissolved before the next experiment.

8 Conclusions and further work

8.1 Concluding remarks

In this thesis, a model based parametric study was successfully conducted and documented. A water model has been optimized to resemble an industrial cell, which contributed to experiments being more realistic and similar to the industry. Natreen was chosen as the experimental powder, successfully resembling alumina in the formation and dissolution of rafts on the bath surface. The performed water model analysis included thorough investigation of the effects of temperature, PSD and bubble frequency.

The water model was optimized successfully with covers for the anode tubes, in addition to a fixed camera and feeder mount. Optimizations to the anode tubes resulted in fewer and larger bubbles, in close similarity to industrial gas-bubbles. With the possibility to calculate the correspondence between gas flow rate and current densities in industrial anodes, water model experiments can be conducted to simulate specific current densities of industrial cell lines. Optimization was also achieved with fixed mounts for the camera and feeder, both contributing to higher reproducibility. A fixed camera mount and the use of black cloth to decrease reflections and glare, provided good conditions for an automated image analysis with high reproducibility. However, a completely automated analysis was not achieved, due to inconsistencies in contrast between rafts and bath.

The amount of research used to find a powder close to alumina in raft formation behavior provided to be more demanding than expected, especially in the crushing process and monitoring PSD. The initial experiments performed to find a powder comparable to the behavior of alumina in industrial cells, was successfully conducted with the discovery of Natreen as a well-suited outcome. Natreen sprinkle sugar, crushed into desired fractions and distributions, replicates the behavior of alumina in the way of forming rafts on top of a liquid surface under certain conditions. The PSD used for Natreen during these experiments is far off the desired PSD used by alumina smelters, and the shape of Natreen particles is also considerably different. Nevertheless, given these physical differences, resemblance was observed and recorded in raft behavior, dispersion, and dissolution.

Results from the experiments indicates that increased bubble frequency (gas flow rate/current density) and temperature reduced the floating time. A high amount of fine particles (fine PSD) was both documented and observed to have the most influence on floating time. Tests with a fine PSD gave a mean floating time between 240 and 550 seconds, in comparison to the coarse PSD-tests with a mean floating time in the range of 35 to 135 seconds. This suggests that a high amount of fine particles have a negative impact on dissolution, which coincides with previous observations, both from the industry and laboratory studies.

The current work demonstrate several promising features and covers several relevant parameters which ultimately can be used for validating numerical models aiming to simulate the real process.

8.2   Further work

To increase the statistical confidence of the results, conduction of additional experiments on the parameter combinations studied in the water model should be considered, as well as utilizing a randomized experimental matrix. Improved methods of crushing powder will increase the efficiency of the experimental process. By using a large ball mill or roll mill, it is possible to crush several liters of powder at once and monitor PSD more closely. More appropriate methods of measuring PSD should also be considered.

Further work on the water model should focus on optimizing light conditions, both on the model itself and its surroundings. This could secure an even contrast threshold between the powder and the bath, and potentially make a fully automated, computer-scripted, image analysis possible. Adjustments that could be considered include an increase in contrast by coloring bath or powder, as well as a range of variations in light conditions such as brightness and/or incoming light angle. To reduce glare from the anode tubes, the curved plates should be painted in a dim black colour. Changes regarding the camera placement, to make the camera able to record the entirety of the bath, could be beneficial. All the improvements however, needs to be recorded and post processed to know which conditions that may truly enhance the threshold-setting-quality.

Because of difficulties with measuring the gas flow rate, variations of this parameter were set without sufficient instruments. A strict measure of the gas flow rate parameter would, through Faraday's law and the ideal gas law, enable a more precise simulation of certain current densities in correspondence to an industrial cell.

References

[1] Merete Tangstad. *Metal production in Norway*. Akademika Publishing, 2013. ISBN: 978-82-321-0241-9.

[2] Roger N. Lumley. *Fundamentals of Aluminium Metallurgy : Production, Processing and Applications*. Woodhead Publishing in Materials. Oxford: Woodhead Publishing, 2011. ISBN: 978-1-84569-654-2. URL: http://search.ebscohost.com/login.aspx?direct=true&db=e000xww&AN=680662&site=ehost-live.

[3] Kai Grjotheim and Halvor Kvande. *Introduction to aluminium electrolysis : understanding the Hall-Héroult process*. 2nd ed. Düsseldorf: Aluminium-Verlag, 1993. ISBN: 3-87017-233-9.

[4] Kitungwa Kabezya, Tom Hara, and Randall Paton. "A review of primary aluminium tapping models". In: *SN Applied Sciences* 1.8 (July 11, 2019), p. 850. ISSN: 2523-3971. DOI: 10.1007/s42452-019-0869-6. URL: https://doi.org/10.1007/s42452-019-0869-6 (visited on 04/25/2020).

[5] Graham Gibbs and France Labrèche. "Cancer Risks in Aluminum Reduction Plant Workers A Review". In: *Journal of occupational and environmental medicine / American College of Occupational and Environmental Medicine* 56 Suppl 5S (2014), S40–S59. DOI: 10.1097/JOM.0000000000000003.

[6] Pascal Lavoie, Mark P. Taylor, and James B. Metson. "A Review of Alumina Feeding and Dissolution Factors in Aluminum Reduction Cells". In: *Metallurgical and Materials Transactions B* 47.4 (Aug. 2016), pp. 2690–2696. ISSN: 1543-1916. DOI: 10.1007/s11663-016-0680-3. URL: https://doi.org/10.1007/s11663-016-0680-3.

[7] Niels Peter Østbø. *Evolution of alpha phase alumina in agglomerates upon addition to cryolitic melts*. Vol. 2002:50. Doktor ingeniøravhandling (Trondheim : online). Trondheim: Norwegian University of Science, Technology, Department of Materials Technology, and Electrochemistry, May 2002. 266 pp.

[8] Barry J. Welch and Gerda I. Kuschel. "Crust and Alumina Powder Dissolution in Aluminum Smelting Electrolytes". In: *JOM* 59.5 (May 2007). Place: New York Publisher: Springer Nature B.V., pp. 50–54. ISSN: 10474838. URL: https://search.proquest.com/docview/232564703?accountid=12870.

[9] Csilla Kaszás et al. "Behavior of Powders on the Surface of a Liquid". In: *Light Metals 2015*. Ed. by Margaret Hyland. Cham: Springer International Publishing, 2016, pp. 639–642. ISBN: 978-3-319-48248-4. DOI: `10.1007/978-3-319-48248-4_107`. URL: `https://doi.org/10.1007/978-3-319-48248-4_107`.

[10] Sindre Engzelius Gylver. *Alumina Dissolution in Cryolite Melts - Formation and Behavior of Rafts*. NTNU, 2018. URL: `http://hdl.handle.net/11250/2576483`.

[11] Youjian Yang et al. "Study on the Dissolution of Alumina in Cryolite Electrolyte Using the See-Through Cell". In: *Light Metals 2015*. Ed. by Margaret Hyland. Cham: Springer International Publishing, 2016, pp. 583–588. ISBN: 978-3-319-48248-4. DOI: `10.1007/978-3-319-48248-4_97`. URL: `https://doi.org/10.1007/978-3-319-48248-4_97` (visited on 05/19/2020).

[12] Ellen H. M. Moors. "Technology strategies for sustainable metals production systems: a case study of primary aluminium production in The Netherlands and Norway". In: *Journal of Cleaner Production* 14.12 (2006), pp. 1121–1138. ISSN: 0959-6526. DOI: `https://doi.org/10.1016/j.jclepro.2004.08.005`. URL: `http://www.sciencedirect.com/science/article/pii/S0959652605000594`.

[13] Alton T. Tabereaux and Ray D. Peterson. "Chapter 2.5 - Aluminum Production". In: *Treatise on Process Metallurgy*. Ed. by Seshadri Seetharaman. Boston: Elsevier, 2014, pp. 839–917. ISBN: 978-0-08-096988-6. DOI: `10.1016/B978-0-08-096988-6.00023-7`. URL: `http://www.sciencedirect.com/science/article/pii/B9780080969886000237`.

[14] Youjian Yang et al. "The Formation and Dissolution of Crust Upon Alumina Addition into Cryolite Electrolyte". In: *JOM* 67.9 (Sept. 2015), pp. 2170–2180. ISSN: 1543-1851. DOI: `10.1007/s11837-015-1525-2`. URL: `https://doi.org/10.1007/s11837-015-1525-2`.

[15] OAR US EPA. *Greenhouse Gas Equivalencies Calculator*. US EPA. Library Catalog: www.epa.gov. Aug. 28, 2015. URL: `https://www.epa.gov/energy/greenhouse-gas-equivalencies-calculator` (visited on 03/19/2020).

[16] Jim P. Kissane. "Optimising alumina feeders in aluminium smelting pots". In: *Department of Mechanical Engineering, University of Wollogong* (1995). URL: `https://ro.uow.edu.au/theses/1589/` (visited on 05/04/2020).

[17] Jomar Thonstad et al. "The Dissolution of Alumina in Cryolite Melts". In: *Essential Readings in Light Metals: Volume 2 Aluminum Reduction Technology*. Ed. by Geoff Bearne, Marc Dupuis, and Gary Tarcy. Cham: Springer International Publishing, 2016, pp. 105–111. ISBN: 978-3-319-48156-2. DOI: `10.1007/978-3-319-48156-2_14`. URL: `https://doi.org/10.1007/978-3-319-48156-2_14`.

[18] Csilla Kaszás et al. "Spreading of Alumina and Raft Formation on the Surface of Cryolitic Bath". In: *Light Metals 2017*. Ed. by Arne P. Ratvik. Cham: Springer International Publishing, 2017, pp. 473–478. ISBN: 978-3-319-51541-0.

[19] Richard G. Haverkamp and Barry J. Welch. "Modelling the dissolution of alumina powder in cryolite". In: *Chemical Engineering and Processing: Process Intensification* 37.2 (1998), pp. 177–187. ISSN: 0255-2701. DOI: `https://doi.org/10.1016/S0255-2701(97)00048-2`. URL: `http://www.sciencedirect.com/science/article/pii/S0255270197000482`.

[20] Sindre Engzelius Gylver et al. "Lab Scale Experiments on Alumina Raft Formation". In: *Light Metals 2020*. Ed. by Alan Tomsett. The Minerals, Metals & Materials Series. Cham: Springer International Publishing, 2020, pp. 659–663. ISBN: 978-3-030-36408-3. DOI: `10.1007/978-3-030-36408-3_89`.

[21] Sindre Engzelius Gylver et al. "The Micro- and Macrostructure of Alumina Rafts". In: *Light Metals 2019*. Ed. by Corleen Chesonis. Cham: Springer International Publishing, 2019, pp. 689–696. ISBN: 978-3-030-05864-7.

[22] Sindre Engzelius Gylver et al. "Alumina Feeding and Raft Formation: Raft Collection and Process Parameters". In: *Light Metals 2019*. Ed. by Corleen Chesonis. Cham: Springer International Publishing, 2019, pp. 659–666. ISBN: 978-3-030-05864-7.

[23] Dawn C. Chesonis and Alfred F. LaCamera. "The Influence of Gas-driven Circulation on Alumina Distribution and Interface Motion in a Hall-Heroult Cell". In: Light Metals, 1990, pp. 211–220.

[24] Thomas Roger et al. "Development of a Mathematical Model to Simulate Raft Formation". In: *Light Metals 2020*. Ed. by Alan Tomsett. The Minerals, Metals & Materials Series. Cham: Springer International Publishing, 2020, pp. 688–695. ISBN: 978-3-030-36408-3. DOI: `10.1007/978-3-030-36408-3_93`.

[25] Véronique Dassylva-Raymond et al. "Modeling the Behavior of Alumina Agglomerate in the Hall-Héroult Process". In: *Light Metals 2014*. Ed. by John Grandfield. Cham: Springer International Publishing, 2016, pp. 603–608. ISBN: 978-3-319-48144-9. DOI: `10.1007/978-3-319-48144-9_102`. URL: `https://doi.org/10.1007/978-3-319-48144-9_102`.

[26] Kristian Etienne Einarsrud. *A Treatise on Interpolar Transport Phenomena*. Accepted: 2014-12-19T11:50:01Z. Norges teknisk-naturvitenskapelige universitet, Fakultet for ingeniørvitenskap og teknologi, Institutt for energi- og prosessteknikk, 2012. ISBN: 978-82-471-3699-7. URL: `https://ntnuopen.ntnu.no/ntnu-xmlui/handle/11250/235008` (visited on 06/02/2020).

[27] Mark Cooksey and William Yang. "PIV Measurements on Physical Models of Aluminium Reduction Cells". In: *TMS Light Metals* 2006 (2006), pp. 359–365.

[28] Sebastien Fortin et al. "Physical Modelling of Bubble Behaviour and Gas Release from Aluminum Reduction Cell Anodes". In: *Essential Readings in Light Metals: Volume 2 Aluminum Reduction Technology*. Ed. by Geoff Bearne, Marc Dupuis, and Gary Tarcy. Cham: Springer International Publishing, 2016, pp. 385–395. ISBN: 978-3-319-48156-2. DOI: `10.1007/978-3-319-48156-2_55`. URL: `https://doi.org/10.1007/978-3-319-48156-2_55` (visited on 06/06/2020).

[29] *ImageJ*. In: *Wikipedia*. Page Version ID: 959348684. May 28, 2020. URL: `https://en.wikipedia.org/w/index.php?title=ImageJ&oldid=959348684` (visited on 06/04/2020).

[30] Microsoft Corporation. *Microsoft Excel. Version 2019 (16.0)*. Sept. 24, 2018. URL: `https://office.microsoft.com/excel`.

[31] Wayne Rasband. *ImageJ. Version 1.53a*. USA: National Institutes of Health, 2020. URL: `http://imagej.nih.gov/ij`.

[32] Sindre Engzelius Gylver. *Simulering av aluminamating ved vannmodellering*. SFI Metal Production, Jan. 1, 2018.

[33] Douglas C. Montgomery. *Design and analysis of experiments*. 8. utg. Pages: xvii, 730. Hoboken, NJ: John Wiley & Sons, Inc, 2013. xvii+730. ISBN: 978-1-118-14692-7.

[34] *MATLAB*. In: *Wikipedia*. Page Version ID: 956129703. May 11, 2020. URL: `https://en.wikipedia.org/w/index.php?title=MATLAB&oldid=956129703` (visited on 06/04/2020).

[35]   *MATLAB. Version 9.7.0.1190202 (R2019b).* Natick, Massachusetts: The Math-Works Inc., 2019.

[36]   Javier Montalt Tordera. *Filled area plot.* MATLAB Central File Exchange. Library Catalog: se.mathworks.com. 2020. URL: `https : / / se . mathworks . com / matlabcentral / fileexchange / 69652 ‑ filled ‑ area ‑ plot` (visited on 06/04/2020).

[37]   *The Solubility Of The Sugars.* Library Catalog: chestofbooks.com. URL: `https:// chestofbooks.com/food/science/Experimental-Cookery/The-Solubility- Of-The-Sugars.html` (visited on 06/15/2020).

A   Calculations between gas flow rate and current density

Bubble producing tubes in the water model simulate the CO_2-production from the
anodes of an industrial cell. By using the ideal gas law and Faraday's law, the gas
flow rate used in water model experiments can be linked to the current density of an
industrial anode.

Ideal gas equation is given:

$$P\,V = n\,R\,T$$

$$n = \frac{P\,V}{R\,T} \tag{A.1}$$

Introducing air flow rate $(\dot{V})$ to the volume:

$$\dot{n_G} = \frac{P\dot{V}}{R\,T} \tag{A.2}$$

Where the following values are used:

- P = 1 atm, pressure at the laboratory.

- T = 293 K, temperature at the laboratory.

- $\dot{V}$ = Air flow used as "high" and "low" during experiments as presented in Table
  6.1, given $[L/s]$ as unit of measurement during these calculations.

- R = 0.08205 $\frac{atm\,L}{mol\,K}$

- n_G = amount of substance

From the laws of Faraday, the equation can be written as:

$$P = \frac{M\,I\,t}{z\,F}$$

$$\frac{P}{M} = \frac{I\,t}{z\,F} \tag{A.3}$$

Where:

$$\frac{P}{M} = n_F \tag{A.4}$$

$$\Rightarrow \quad n_F = \frac{I \, t}{z \, F} \tag{A.5}$$

To find the rate of change in the amount of substance, the expression is derived with
respect of time:

$$\dot{n_F} = \frac{dn_F}{dt} = \frac{I}{z \, F} \tag{A.6}$$

- I = is the current in ampere [A]

- z = 4, is the number of electrons included in the anode reaction from Eq. (1.2)

- F = 98 500 C/mol, Faraday's constant

To find the current consumption corresponding to the bubble frequency (gas flow):

$$\dot{n_G} = \dot{n_F} \tag{A.7}$$

$$\frac{P \, \dot{V}}{R \, T} = \frac{I}{z \, F} \tag{A.8}$$

$$\Rightarrow \quad I = \frac{P \, \dot{V} \, z \, F}{R \, T} \tag{A.9}$$

The current consumption can then be calculated for the "low" and "high" gas flow rates
used in water model experiments from Eq. (A.9):

$$I_{low} = \frac{1 \, atm \times 1.25 \, L/sec \times 4 \times 98500 \, C/mol}{0.08205 \, \frac{atm \, L}{mol \, K} \times 293 \, K} = \underline{20 \; 486 \; A} \tag{A.10}$$

$$I_{high} = \frac{1 \, atm \times 3.3 \, L/sec \times 4 \times 98500 \, C/mol}{0.08205 \, \frac{atm \, L}{mol \, k} \times 293 \, K} = \underline{53 \; 176 \; A} \tag{A.11}$$

Selecting an anode area in correlation to the water model and an average anode size
used in industrial cells [26, p.46], the cross-sectional area of the anode (A_a) is set to
$0.9\,m \ \times \ 1.6\,m = 1.44\,m^2 = A_a$. To further calculate the current density (J) to each of
the two anode tubes used in the water model, the current consumption is divided by
two in addition to anode area A_a:

$$J = \frac{I}{2 \times A_a} \tag{A.12}$$

$$J_{low} = \frac{20\,486\ A}{2 \times 1.44\ m^2} = \underline{\underline{7\,113\ A/m^2}} \tag{A.13}$$

$$J_{high} = \frac{53\,176\ A}{2 \times 1.44\ m^2} = \underline{\underline{18\,463\ A/m^2}} \tag{A.14}$$

Table A.1: Calculated results form the correlation between gas flow rate and current
density.

Gas Flow [L/min]	Current density [A/cm²]
75	0.7
200	1.8

B   Illustration of dissolution rates
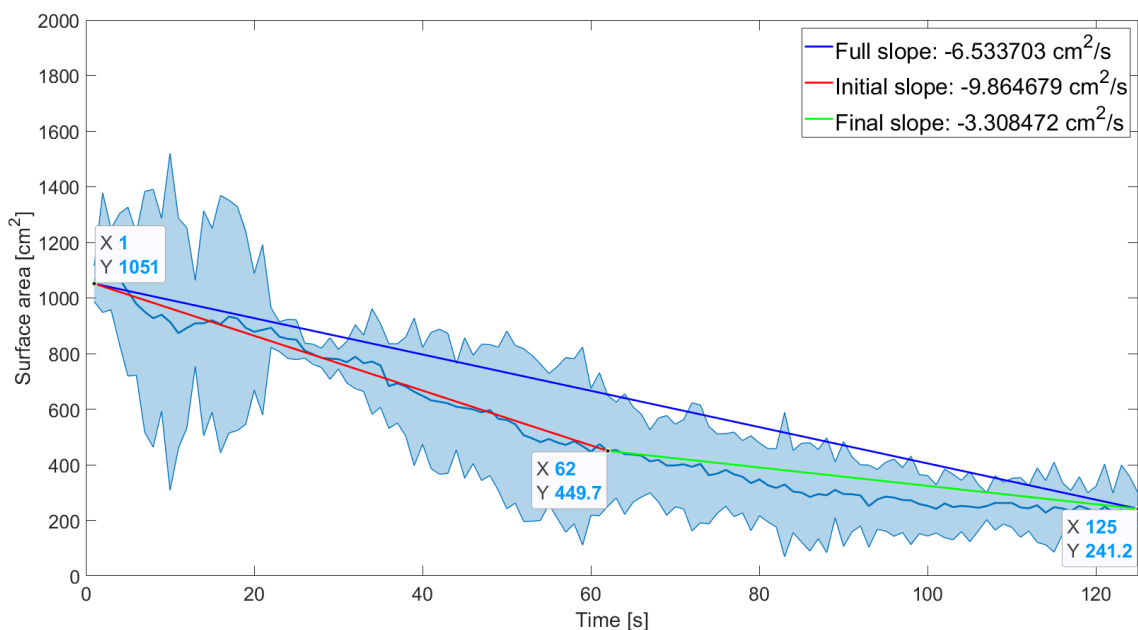
Figure B.1: Illustration showing calculation of dissolution rates.

The dissolution rates of the experiments are calculated from three points (start, halfway, end) in each graph. Lines can then be drawn between points, which enables easy calculation of the slope gradients. The slope of each line equals to the rate of which the powder dissolves (dissolution rate), measured in cm^2/s or $\%/s$. An example of points and lines used for the calculations is shown in Figure B.1. The blue line shows the full slope, representing the dissolution rate of the entire duration. The initial slope is marked in red, whereas the final slope is marked in green, representing the dissolution rate of the first and second half, respectively.

C   Location of the camera blind spot

Figure C.1: Simplified illustration showing the approximate extent of the camera blind spot (orange area) present in the water model.
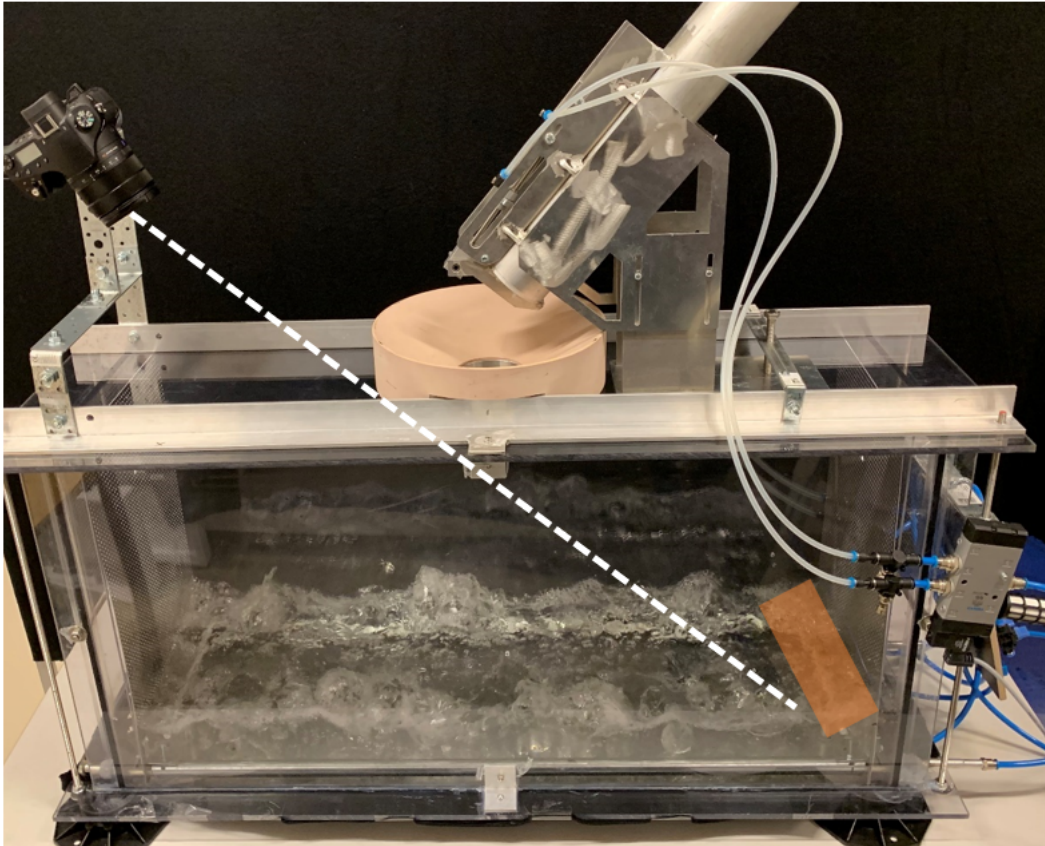
Figure C.1 shows the approximate extent of the camera blind spot present in the water model, shown as a orange square on the bath surface. The blind spot is located near the short end of the model, on the opposite end of where the camera is placed.

D   Calculations of solubility limit

For the coarse and fine batch used in these experiments, following densities have been measured:

Table D.1: Density of the fine and coarse batch.

Batch	Density
-	[kg/L]
Fine	0.28
Coarse	0.25

As approximately one liter of powder is added for each experiment and water is changed every third experiment. A total of $3\ L \times 0.28\ kg/L = 0,84\ kg$ and $3\ L \times 0.25\ kg/L = 0.75\ kg$ is added for the fine and coarse batch, respectively, for every parameter adjusted.

From the measurements of the water model in Section 4.12, around 31 L of water is added as bath for every parameter tested. Giving a total Natreen concentration of $0.84\ kg \div 31\ L = \underline{\underline{0.027\ kg/L}}$ and $0.75\ kg \div 31\ L = \underline{\underline{0.024\ kg/L}}$ for the fine and the coarse batch, respectively.

In comparison to the solubility limit for sugar [37]:

Table D.2: Solubility limit of sugar [37].

Temperature	Solubility limit
[°C]	[kg/L]
0	1.8
10	1.9

Maximum concentration of Natreen during experiments per parameter adjustment in the fine and coarse batch, respectively, contains approximately 1.3% and 1.5% of the solubility limit for sugar in water at the different temperatures.

E   Image of agglomerate

Figure E.1: Image showing agglomerate sticking to the rigid cathode (bottom plexiglas). This can also be seen in a video at (`https://www.youtube.com/watch?v=oa8utBlcrvE`).

Figure E.1 shows an agglomerate at the bottom of the water model. This agglomerate is marked with a red circle and can also be seen in the video linked in the figure.

F   Individual graphs of experiments 1-3
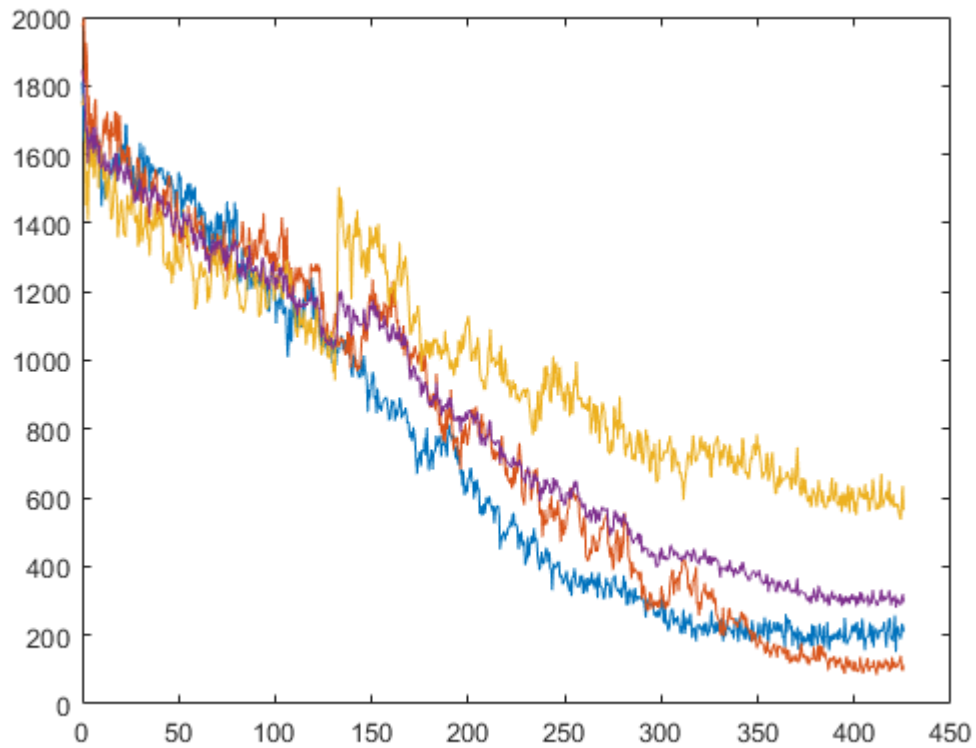
Figure F.1: Individual graphs of experiments 1-3 plotted as cm² against time (s). Average values plotted as a purple line. Blue line being the first experiment, yellow the second and orange the third.

The irregularities in Figure 6.1 originates in the yellow line shown in Figure F.1. This line represents the second experiment and influences both the average values and confidence interval of Figure 6.1.

G   Popular Science Article

Aluminium Production: From Ore to Metal and Back Again

Simen Bekkevoll, Simen Aase, Sigmund A.K. Forberg

Norwegian University of Science and Technology
Faculty of Natural Science
Department of Material Science and Engineering

Aluminium is the third most abundant element in the earth's crust, and the most abundant metallic element [4]. Aluminium is always found combined to other chemical compounds, such as oxides, silicates, and different metals. The energy-intensive production process of aluminium involves two independent processes. First, the Bayer-process which transform the ore, called bauxite, to alumina, and the Hall-Héroult-process, in which alumina is electrolytically reduced to produce pure liquidous aluminium. Aluminium is a widely used metal in today's society, found in everyday consumer goods and highly technical alloys. This article explains how aluminium is produced from the ore, to pure aluminium through the Bayer- and Hall-Héroult-process, and how it can be recycled endless times without losing its properties.

Figure 1: *Charles Martin Hall (left) and Paul L.T. Héroult (right) [3].*

The production process
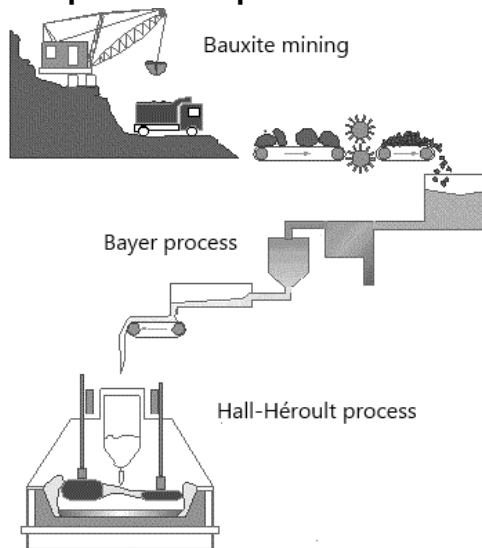
Figure 2: *A schematic flow chart of the aluminium production process as a whole. From the ore to alumina to aluminium metal [1]*

History

Iron, lead, and copper are examples of metals that has been used in over 3000 years. The existence of aluminium however, was not recognized until 1808, only being in commercial use in the last 150 years [4]. This is because aluminium requires a large amount of energy and high temperatures to reduce the raw material, alumina, to aluminium. The commercial production process used by aluminium smelters today was invented in 1886, almost simultaneously, by Charles Martin Hall in the United states and Paul L.T. Héroult of France, and is called the Hall-Héroult-process. This provided the opportunity for economical aluminium production in the 1890's, with the additional Bayer process, invented by Karl Joseph Bayer in 1888, where the extraction of alumina from the ore is performed.

Form the ore to alumina: The Bayer-process

Aluminium production starts with the ore called bauxite, which is further extracted to alumina. It was first discovered in a small town in France, called Les-Baux, hence the name Bauxite. Bauxite deposits are mainly found in a wide belt around equator, relatively close to the surface, typically containing about 40-60% of alumina[4]. After bauxite is mined it is refined to separate the alumina, consisting of aluminium and oxygen by the chemical formula Al_2O_3, by using a hot solution of lye and lime [6]. This mixture is further heated and filtered, where the remaining alumina is dried, to a white powder that looks like table salt.

Figure 3: *Bauxite [6]*

Figure 4: *Alumina [6]*

From alumina to metal: The Hall-Héroult-process

The alumina is reduced in an electrochemically to molten aluminium by the Hall-Héroult process. Where alumina is dissolved in a molten salt bath, mainly consisting of cryolite, at a temperature of around 960 °C [4]. Alumina is the raw material of the process, along with carbon and electrical energy, where the oxygen bound to the aluminium cations is separated to form CO_2 with the reduced carbon from the anodes. The liquidous aluminium lays in the bottom of the aluminium production cell and needs to be tapped with regular time intervals. Tapped aluminium, referred to as primary aluminium, is further transported to a cast house where it is machined into desired products.
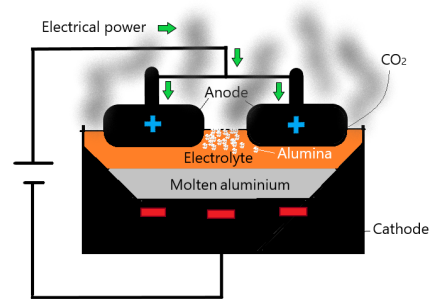

Figure 5: *Illustration of an aluminium production cell.*

Properties and use

Aluminium is second in use by the industry behind iron, and has many useful properties. It is light, only one third the density of steel, it has a high conductivity for heat and electricity, and can withstand corrosion in most environments. It can be casted or fabricated into a wide range of consumer goods or mixed with other metallic elements to produce wrought aluminium alloys. Approximately two-thirds of produced aluminium is used in wrought forms today, where aluminium products are alloyed to give them desired combinations of properties [4]. However, the near-to-pure aluminium is substantially used in foils and electrical cables, representing a large portion of the aluminium products manufactured today.

Figure 6: *Different uses and appliances for aluminium [2].*

Emissions and energy demand

From the processes explained, it possible to imagine that all these steps is highly energy-intensive, with a high amount of greenhouse gas emissions and other waste products. For the whole production process; four tons of dried bauxite is required to produce two tons of alumina, from which one ton of aluminium is extracted [4]. In addition to this, about 1.5 tons of CO_2 is produced form the process in total [5]. The Bayer-process also produces an environmentally challenging

by-product called "red mud", which is stored in large long-term storage facilities [7].
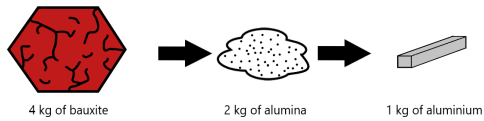

Figure 7: *Input to output of the aluminium production process*

As the global energy demand steadily increases, it is desirable for the aluminium smelters to increase their energy efficiency for better utilization of power [4]. It is also advantageous that the electricity used in the process is provided by renewable energy sources, as greenhouse gas emissions has received increased attention in recent years. If the energy used in the process comes from fossil fuels, the CO_2 emissions from energy production will contribute much more to greenhouse gas emissions than from the electrolysis process [5]. This makes countries rich in renewable energy sources, like Norway and Iceland, a desirable place for aluminium production [5]. Although, a lot of technological improvements has been invented by the industry to reduce energy consumption and emissions through the years, further reduction is needed.

Recycling

One of aluminum's greatest characteristics is that it can be recycled numerous times without losing its mechanical properties. This is because the recycling process consists of only one step, which is to re-melt the metal. The recycling process demands only 5% of the energy that is needed to produce primary aluminium from bauxite [5]. This means that the aluminium production can be an environmentally friendly material in the long run, every time it is recycled. Some challenges in the recycling process is to separate the elements from the alloys, which is solved today by mixing recycled aluminium with new primary aluminium from the electrolysis. Approximately 75% of the aluminium ever produced on the earth is still in use today[5]!
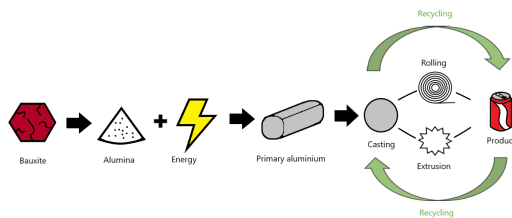

Figure 8: *Aluminium lifecycle, from bauxite to alumina, to metal with electrical energy, to finished product and back trough recycling.*

Future of aluminium

As the global demand for strong, light weight, long lasting, environmentally friendly, and recyclable materials steadily increase, aluminium is a contributing element although being difficult to extract. By 2040, the global aluminium demand is predicted to be around 90 million tones of primary aluminium, in addition to 70 million tons of recycled aluminium [7].

To reach the requirements of a more sustainable production, efficient solutions needs to be invented to handle both current and future challenges in the industry. Future aluminium production is expected to be more autonomic, with robots doing the remaining manual labor at the production sites. Research within alternative production methods are in development but is still facing challenges for an optimal operation. The energy efficiency is expected to increase with innovations of better utilization of power, and the CO_2-emissions is imagined to be captured and stored by carbon capture. In addition it needs to reduce the waste of by-products and other materials used in the production process [5].

Bibliography

[1] Reza Beheshti. "Sustainable Aluminium and Iron Production". PhD thesis. 2017.

[2] *Hulamin Integrated Report 2016: The business > Products and applications of aluminium.* URL: https://www.hulamin.com/iar2016/Business_products_applications_aluminium.html (visited on 06/15/2020).

[3] *In search of aluminum.* URL: https://riotinto.is/?PageID=121 (visited on 06/15/2020).

[4] Roger Lumley. *Fundamentals of Aluminium Metallurgy: Production, Processing and Applications.* Woodhead Publishing in materials. GB: Woodhead Publishing Ltd, 2011. ISBN: 978-1-84569-654-2.

[5] *Metal production in Norway.* Oslo: Akademika Publ, 2013. ISBN: 978-82-321-0241-9.

[6] *Slik lages aluminium.* Library Catalog: www.hydro.com. URL: https://www.hydro.com/no-NO/om-aluminium/slik-lages-aluminium/ (visited on 06/16/2020).

[7] David S. Wong and Pascal Lavoie. "Aluminum: Recycling and Environmental Footprint". In: *JOM* 71.9 (Sept. 2019), pp. 2926–2927. ISSN: 1047-4838, 1543-1851. DOI: 10.1007/s11837-019-03656-9. URL: http://link.springer.com/10.1007/s11837-019-03656-9 (visited on 06/16/2020).

H Risk assessment

Kartlegging av risikofylt aktivitet

	Utarbeidet av	Nummer	Dato
NTNU	HMS-avd.	HMSRV2601	22.03.2011
	Godkjent av	Side	Erstatter
HMS	Rektor		01.12.2006

Enhet: IMA **Dato:** 20.04.2020

Linjeleder: Tor Grande

Deltakere ved kartleggingen (m/ funksjon): Simen Aase (Student), Simen Bekkevoll (Student), Sigmund Forberg (Student), Sindre E. Gylver
(Ansv. veileder, student, evt. medveiledere, evt. andre m. kompetanse) (Stipendiat), Kristian Etienne Einarsrud (Ansvarlig veileder)

Kort beskrivelse av hovedaktivitet/hovedprosess: Simulering av aluminiumating i en vannmodell

Er oppgaven er rent teoretisk? *(JA/NEI)* NEI *"JA" betyr at veileder innestår for at oppgaven ikke innholder noen aktiviteter som krever risikovurdering*

Dersom "JA": Beskriv kort aktiviteten i kartleggingsskjemaet under. Risikovurdering trenger ikke å fylles ut.

Signaturer: *Ansvarlig veileder:* *Student:*

ID nr.	Aktivitet/prosess	Ansvarlig	Eksisterende dokumentasjon	Eksisterende sikringstiltak	Lov, forskrift o.l.	Kommentar
1	Fylling og tapping av vann	SEG				
2	Håndtere tørris	SEG	Datablad	Vernebriller, hansker, labfrakk		
3	Håndtere is	SEG				
4	Jobbe med trykkluft	SEG		Vernebriller		
5	Håndtere avkjølt pulver	SEG		Hansker		
6	Smittefare (Coronavirus)	SEG				

88

NTNU		Risikovurdering		Utarbeidet av	Nummer	Dato
HMS /KS				HMS-avd.	HMSRV2603	04.02.2011
				Godkjent av	Side	Erstatter
				Rektor		09.02.2010

Enhet: *IMA*   **Dato:** *20.04.2020*

Linjeleder: *Tor Grande*

Deltakere ved risikovurderingen (m/ funksjon): Simen Aase (Student), Simen Bekkevoll (Student), Sigmund Forberg (Student), Sindre E. Gylver (Stipendiat), Kristian Etienne Einarsrud (Ansvarlig veileder)

(Ansv. veileder, student, evt. medveiledere, evt. andre m. kompetanse)

Risikovurderingen gjelder hovedaktivitet: Simulering av aluminiumsmelting i en vannmodell

Signaturer: *Ansvarlig veileder:*   *Student:*

ID nr.	Aktivitet/prosess fra kartleggingsskjemaet	Mulig uønsket hendelse	Vurdering av sann-synlighet (1-5)	Vurdering av konsekvens				Risiko-verdi (menn-eske)	Kommentarer/ status Forslag til tiltak
				Menneske (A-E)	Ytre miljø (A-E)	Øk./materiell (A-E)	Om-dømme (A-E)		
1	Fylling og tapping av vann	Ingen							
2	Håndtere tørris	Kontakt på hud og øyne	2	B				B2	
2	Håndtere tørris	Dannelse av farlige mengder CO_2 gass	1	C				C1	Det er god ventilasjon i rommet
3	Håndtere is	Frostskader	1	B				B1	Spade/hansker brukes
4	Jobbe med trykkluft	Splinter som følge av overtrykk	1	B				B1	Vernebriller forhindrer at splinter kommer inn i øyne
5	Håndtere avkjølt pulver	Frostskader på hendene ved håndtering	1	B				B1	Hansker skal benyttes
6	Smittefare	Coronavirus	3	B				B3	Opprettholde minst 2m avstand. Jevnlig desinfisering av overflater og håndvask med såpe. Fordele oppgaver slik at samme person har fast ansvar for samme oppgave. Evt bruk av maske og hansker. Sperre arbeidsstasjon for utenforstående Benytte personlig verneutstyr som desinfiseres.

S.Aase, S.Bekkevoll, S.Forberg

A Model Based Parametric Study of Alumina Feeding and Dissolution

NTNU
Norwegian University of
Science and Technology